

Published in final edited form as:

Nat Cardiovasc Res. 2022 May ; 1(5): 476–490. doi:10.1038/s44161-022-00061-5.

Apelin-driven endothelial cell migration sustains intestinal progenitor cells and tumor growth

Jeremiah Bernier-Latmani^{1,†}, Christophe Cisarovsky^{1,†}, Samantha Mahfoud¹, Simone Ragusa¹, Isabelle Dupanloup³, David Barras^{1,3}, François Renevey⁴, Sina Nassiri^{2,3}, Pascale Anderle³, Mario Leonardo Squadrito², Stefanie Siegert⁴, Suzel Davanture¹, Alejandra González-Loyola¹, Nadine Fournier³, Sanjiv A. Luther⁴, Rui Benedito⁵, Philippe Valet⁶, Bin Zhou⁷, Michele De Palma², Mauro Delorenzi^{1,3}, Christine Sempoux⁸, Tatiana V. Petrova^{1,2,*}

¹Department of Oncology, Ludwig Center for Cancer Research Lausanne and University of Lausanne, Lausanne, Switzerland

²Swiss Institute for Experimental Cancer Research (ISREC), School of Life Sciences, EPFL, Lausanne, Switzerland

³Bioinformatics Core Facility, SIB Swiss Institute of Bioinformatics, Lausanne, Switzerland

⁴Department of Biochemistry, University of Lausanne, Lausanne, Switzerland

⁵Centro Nacional de Investigaciones Cardiovasculares (CNIC), Madrid, Spain

⁶Institut RESTORE, UMR 1301-INSERM, 5070-CNRS, Université Paul Sabatier, Université de Toulouse, Toulouse, France

⁷State Key Laboratory of Cell Biology, CAS Center for Excellence in Molecular Cell Science, Shanghai Institute of Biochemistry and Cell Biology, Chinese Academy of Sciences, Shanghai, China

⁸Institute of Pathology, Lausanne University Hospital and University of Lausanne, Lausanne, Switzerland

Abstract

Stem and progenitor cells residing in the intestinal crypts drive the majority of colorectal cancers (CRCs), yet vascular contribution to this niche remains largely unexplored. VEGFA is a key driver of physiological and tumor angiogenesis. Accordingly, current anti-angiogenic cancer therapies target the VEGFA pathway. Here we report that in CRC expansion of the stem/progenitor

Users may view, print, copy, and download text and data-mine the content in such documents, for the purposes of academic research, subject always to the full Conditions of use: <https://www.springernature.com/gp/open-research/policies/accepted-manuscript-terms>

*Corresponding author. tatiana.petrova@unil.ch.

†Co-first authors

Author contributions

JBL and TVP designed the study; JBL, CC, SM, SR, ID, DB, FR, SN, PA, MLS, SS, SD, AGL, NZ, conducted experiments, acquired, and analyzed data; SAL, RB, PV, BZ, MDP, MD and CS provided reagents and samples; JBL and TVP wrote the manuscript. All authors discussed the results.

Competing interests

TVP receives research funding from Roche for an unrelated project. All other authors declare no conflict of interest.

pool in intestinal crypts requires VEGFA-independent growth and remodeling of blood vessels. Epithelial transformation induced expression of the endothelial peptide apelin, directs migration of distant venous endothelial cells towards progenitor niche vessels ensuring optimal perfusion. In the absence of apelin, loss of injury-inducible PROX1+ epithelial progenitors inhibited both incipient and advanced intestinal tumor growth. Our results establish fundamental principles for the reciprocal communication between vasculature and the intestinal progenitor niche and provide a mechanism for resistance to VEGFA-targeting drugs in CRCs.

Stem and progenitor cells reside in specialized niches that maintain self-renewal while producing differentiated cells. Niche-associated parameters include a unique cellular architecture, defined growth factor gradients, and distinct oxygen pressure. Because hyperplastic stem/progenitor cell growth drives cancer initiation and progression, understanding mechanisms regulating their niches may provide novel therapeutic strategies. However, idiosyncratic properties of organ-specific progenitor niches make a “one-size-fits-all” strategy to target these cells elusive.

The intestinal epithelium is partitioned into spatially segregated stem/progenitor and differentiated compartments. Crypt-housed stem/progenitor cells renew the epithelium through constant Wnt signaling-driven proliferation and production of differentiated daughter cells¹. Uncontrolled stem/progenitor proliferation drives most colorectal cancers (CRCs). Loss-of-function mutations in *APC* are the most common driver of CRC and result in aberrant Wnt signaling, crypt overgrowth, and establishment of Wnt^{high} CRC stem/progenitor niches². Blood vessels are part of this niche and were reported to provide Notch ligands to maintain epithelial cell stemness³. However, mechanisms of vascular regulation in the stem/progenitor niche remain largely unexplored.

During development rapid expansion of the blood vasculature is driven through VEGFA signaling, which promotes endothelial cell proliferation, migration, and survival. In adults, VEGFA is a key driver of angiogenesis associated with wound healing and tumor growth. Accordingly, current anti-angiogenic cancer therapies mostly target the VEGFA pathway⁴. However, many cancers are intrinsically resistant to VEGFA signaling blockade. This includes a major subset of CRC tumors, driven by high Wnt signaling and epithelial progenitor proliferation⁵⁻⁷. Yet, paradoxically, at steady-state, intestinal blood and lymphatic vessel maintenance are VEGF-dependent^{8,9}. Here, we investigated the mechanisms regulating blood vessel morphogenesis in the CRC progenitor niche. We show that normal and transformed crypt stem/progenitor cells, and associated vessels, are VEGFA-independent and normoxic. Rather, progenitor cell vasculature is replenished through apelin-dependent endothelial cell migration from distant venous vessels to ensure stable niche perfusion and normoxia.

Results

Low VEGFA signaling and normoxia are hallmarks of Wnt^{high} CRC

CRC classification based on gene expression revealed 4 distinct molecular sub-types (CMSs)⁵. *APC* loss-of-function mutations are the most common drivers of CRC and result

in aberrantly high Wnt signaling and establishment of Wnt^{high} CRC progenitor niches². However, Wnt^{high} CRC tumors (CMS2 subtype) have low VEGFA signaling⁵ and patients with Wnt^{high} CRC are less sensitive to anti-VEGFA therapy^{6,7}. These observations indicate that Wnt^{high} CRC tumors are intrinsically resistant to VEGFA blockade. To gauge the contribution of Wnt signaling to angiogenesis in human CRC, we established a Wnt activation score based on expression levels of Wnt target genes¹⁰ in 2,275 CRC tumors (Fig. 1a, Supplementary Table 1). In agreement with Guinney et al.⁵, the majority of CMS2 tumors were Wnt^{high} and the majority of CMS1 tumors were Wnt^{low} (Extended Data Fig. 1a). Furthermore, as reported⁵, CMS2 tumors had significantly lower angiogenic scores than CMS1 tumors, and Wnt activation scores were negatively correlated with VEGFA signaling (Fig. 1b, c and Extended Data Fig. 1b, c). Hypoxia and glycolysis signatures were under-represented in Wnt^{high} CRCs, whereas oxidative phosphorylation and peroxisome signatures were enriched (Fig. 1d; full data Supplementary Fig. 1, 2; Supplementary Table 2, 3), suggesting that metabolic processes requiring high O₂ consumption are dominant in progenitor enriched Wnt^{high} tumors.

To corroborate observations from the transcriptome analysis, we analyzed human primary colon adenocarcinomas by immunohistochemistry (Supplementary Table 4). As previously shown^{11–13}, Wnt^{high} tumors were identified by robust nuclear β-CATENIN and expression of the direct WNT target gene PROX1 (Fig. 1e, f). Although there was no difference in vessel density (Fig. 1g, i) vascular ESM1, a marker for active VEGFA signaling¹⁴, was significantly lower in Wnt^{high} compared to Wnt^{neg} tumors (Fig. 1h, j), confirming blood vessels in Wnt^{high} human CRCs have lower VEGFA signaling activation. To analyze the relationship between Wnt^{high} progenitor cells and VEGFA signaling, we used expression of PROX1 to identify areas enriched in progenitors (Wnt^{high}-Pro) or differentiated (Wnt^{high}-Diff) cancer cells (Extended Data Fig. 1d). Wnt^{high}-Pro areas had significantly lower vessel density and ESM1 expression compared to Wnt^{high}-Diff areas. In contrast, Wnt^{neg} tumors had relatively homogenous vessel density and ESM1 expression (Extended Data Fig. 1e-h). Overall, analysis of human CRCs shows that VEGFA-independent vasculature and normoxia are intrinsic properties of the Wnt^{high} CRC progenitor niche.

The normal progenitor cell niche is VEGFA-independent

To understand mechanisms underlying anti-correlative compartmentalization of the progenitor niche and VEGFA signaling we turned to whole-mount immunostaining of adult mouse small intestine vasculature. Small intestinal crypts house epithelial stem and progenitor cells while villi contain differentiated epithelial cells¹. Villus blood vasculature was denser and more branched compared to crypt vessels and displayed filopodia characteristic of angiogenic vessels (Fig. 2a and Extended Data Fig. 2a). Accordingly, VEGFA protein was restricted to the villus and villus capillaries expressed higher ESM1 (Extended Data Fig. 2b, c). These observations agree with previous findings that villus capillaries are VEGFA-dependent^{8,15} and *Vegfa* transcription is restricted to villi¹⁶. VEGFA expression is driven by hypoxia¹⁷, and differentiated epithelial cells of the small intestine and colon are hypoxic¹⁸. However, crypts, but not villi, were normoxic in the small intestine and colon (Extended Data Fig. 2d, e).

VEGFA promotes endothelial cell proliferation, migration, and filopodia formation. Treatment with the anti-VEGFR2 blocking antibody DC101¹⁹ decreased capillary branching, filopodia number, and ESM1 expression in villus vessels, whereas crypt vessel length and branching remained unchanged (Extended Data Fig. 2f-k). Importantly, VEGFR2 blockade did not decrease crypt length nor crypt epithelial cell proliferation (Fig. 2b-d). Thus, crypt-associated vasculature is VEGFA-independent and blocking VEGFA signaling alters vascular parameters in the villus without affecting epithelial cell proliferation in the crypt. These observations portray a model in which normal intestinal stem cells/progenitors are normoxic and surrounded by VEGFA-independent blood vessels, whereas the differentiated intestinal epithelium is hypoxic and associated with VEGFA-dependent villus capillaries (Extended Data Fig. 2l).

Transformed progenitors expand independently of VEGFA

We next asked if VEGFA was necessary for pathological progenitor cell expansion. In *Apc^{fl/fl}; Villin-CreERT2 (Apc^{IEC})* mice, tamoxifen administration induces *Apc* loss-of-function in the intestinal epithelium, resulting in acute expansion of the progenitor compartment, modeling incipient CRC (Fig. 2e)²⁰. Progenitor cell expansion was accompanied by an overall increase in non-sprouting crypt capillary length and decreased vessel branching (Extended Data Fig. 3a-c). Similarly, in *Apc^{min/+}; Lgr5-EGFP-CreERT2* adenomas, capillaries adjacent to transformed GFP⁺ progenitors²¹ resembled expanded crypt vessels (Extended Data Fig. 3d). Consistent with a non-sprouting vascular phenotype, intestinal *Vegfa* was not elevated in *Apc^{IEC}* mice (Extended Data Fig. 3e).

To examine the effect of VEGFA signaling inhibition on transformed progenitors, we treated *Apc^{IEC}* or *Apc*-proficient (wild-type, WT) mice with DC101 or control antibodies (Fig. 2f). VEGF inhibition reduced total intestinal vessel length in *Apc^{IEC}* mice (Fig. 2g-i). However, vessel regression was confined to villus capillaries and vessel length remained unchanged in the expanded crypts (Fig. 2g, i). DC101 blocked endothelial cell proliferation in WT villi, however, there was only a modest decrease of Ki67⁺ endothelial cells in DC101-treated *Apc^{IEC}* mice (Fig. 2j, k), despite reduction in expression of the VEGFA target ESM1 (Extended Data Fig. 2j, k and 3f). Crypt expansion and proliferation were not different between control- and DC101-treated *Apc^{IEC}* mice (Fig. 2j, l, m), confirming that Wnt-driven pathological progenitor cell expansion is unhindered by VEGFR2 signaling blockade.

To test the effect of VEGFR2 blockade in CRC precursor lesions, we injected a single dose of tamoxifen in *Apc^{fl/fl}; Lgr5-EGFP-CreERT2* mice to develop progenitor-rich adenomas²¹. After 6 weeks, we administered DC101 for 2 weeks until mouse sacrifice. DC101 blocked VEGFA signaling (Extended Data Fig. 3g), however, there was no difference in vessel density (Extended Data Fig. 3g, h), number or size of adenomas (Extended Data Fig. 3i-k) and frequency of *Lgr5*-GFP⁺ stem cells between DC101 and control-treated mice (Extended Data Fig. 3i, l). These results demonstrate that VEGFA signaling blockade does not impair crypt-associated blood vessels and progenitor cells during the early stages of CRC development.

We examined the relative O₂ status in crypts and villi of DC101-treated *Apc*^{IEC} mice by staining for pimonidazole adducts and HIF1 α . Only KRT20⁺ differentiated intestinal epithelial cells were hypoxic, whereas expanded crypt cells were normoxic, indicating efficient O₂ diffusion in the rapidly expanding progenitor niche (Fig. 2n). Similarly, hypoxia was restricted to KRT20⁺ differentiated epithelial cells in *Apc*^{min/+} adenomas whereas hyperplastic crypts were normoxic (Extended Data Fig. 3m, n).

We next assessed the relationship between stem/progenitor cells and blood vessels in mouse models of advanced CRC. Along with *APC*, *KRAS* and *TP53* are commonly mutated in human CRCs⁵. Therefore, we generated intestinal organoids from *Apc*^{fl/fl}; *Kras*^{G12D}; *p53*^{fl/fl}; *Villin-CreERT2* (AKP) mice. AKP organoid tumors contain a high proportion of transformed stem/progenitor cells, characterized by nuclear β -catenin localization and expression of Wnt target genes *Axin2*, *Prox1* and *Lgr5*^{1,12}. In contrast, the murine colon adenocarcinoma cell line MC38²² lacked nuclear β -catenin and Wnt signaling (Extended Data Fig. 4a, b). To explore CRC dependence on VEGFA signaling, we treated mice carrying established subcutaneous AKP organoid or MC38 tumors with DC101 or control IgG. As expected²³, the volume and weight of MC38 tumors, as well as cancer cell proliferation, were significantly decreased after DC101 treatment (Extended Data Fig. 4c, d). However, DC101 did not decrease the proliferation rate or expansion of AKP organoid-derived tumors (Fig. 3a, b).

Control MC38 and AKP tumors had comparable vascular density (Extended Data Fig. 4e, f). However, control AKP tumors displayed a significantly lower proportion of ESM1⁺ blood vessels and Ki67⁺ endothelial cells than MC38 tumors (Extended Data Fig. 4g-j). In line with higher VEGFA signaling, DC101-treated MC38 tumors had reduced blood vessel density compared to controls and AKP tumors (58% vs 33%, $p=0.0014$; Extended Data Fig. 4e, f). The proportion of CD44⁺ and PROX1⁺ CRC progenitors^{11,12,24} was not decreased after DC101 treatment (Fig. 3c), indicating that VEGFA signaling blockade neither hinders tumor progenitor maintenance nor AKP tumor growth.

AKP tumors harbored areas with either high or low progenitor cell numbers (Fig. 3d), recapitulating the intratumoral heterogeneity observed in human Wnt^{high} CRC tumors². We also observed compartmentalized vascular phenotypes, with lower vessel density and VEGFA signaling associated with CD44⁺ AKP progenitors (Fig. 3d). CD44⁺ AKP tumor progenitor cells were less hypoxic than CD44^{neg} cancer cells and did not become more hypoxic after VEGFA signaling blockade (Fig. 3e-g). AKP tumor growth was not affected by endothelial-specific ablation of VEGFR2, while growth of MC38 tumors was prevented, further confirming VEGFA-independent growth of AKP organoids (Extended Data Fig. 4k-m).

To verify that repressed VEGFA signaling was a feature of high Wnt signaling tumors we analyzed intestinal tumors from mice with deletion of *Prox1* in addition to *Apc* and *Tp53* (*Apc*^{fl/fl}; *p53*^{fl/fl}; *Prox1*^{fl/fl}; *Vil-CreERT2*, APP). PROX1 is induced in transformed intestinal epithelial cells and maintains high Wnt signaling^{11,13,25} and APP tumors display increased vessel density as compared to Wnt^{high} *Apc*^{fl/fl}; *p53*^{fl/fl}; *Vil-CreERT2* (AP) tumors²⁵. Vascular ESM1 expression was significantly higher in APP tumors (Extended Data Fig.

4n), indicating high Wnt signaling correlates with low VEGFA signaling in mouse models of CRC. Altogether, results from mouse models reinforce observations from human CRC that Wnt^{high} progenitor cells are maintained in well perfused, VEGFA-independent niches.

Acute progenitor expansion induces endothelial apelin

To determine mechanisms of VEGFA-independent vascular maintenance in the crypt, we examined genes differentially expressed in intestinal endothelial cells isolated from WT or *Apc*^{IEC} mice (Extended Data Fig. 5a, b). Apelin (*Apln*) was the most induced protein-encoding transcript in *Apc*^{IEC} intestinal endothelial cells (Fig. 4a and Extended Data Fig. 5c, d). APLN, a ligand for the endothelial-specific G-protein-coupled receptor APJ (*Aplnr*), is expressed in angiogenic tip cells and endomucin^{high} bone-marrow endothelium. APLN sustains angiogenic responses, but also promotes blood vessel enlargement and maturation, arterio-venous alignment and non-angiogenic retina vessel remodeling²⁶⁻³¹.

In situ hybridization confirmed increased endothelial *Apln* expression during stem/progenitor cell expansion (Fig. 4b and Extended Data Fig. 5e). To determine the location and identity of *Apln*-expressing endothelial cells, we analyzed *Apln-CreERT2; mTmG* reporter mice³². Twenty-four hours after induction of recombination, the majority of GFP⁺ endothelial cells were in villi, whereas about 10% of GFP⁺ endothelial cells were in crypts (Fig. 4c, d). Around 85% of GFP⁺ endothelial cells co-stained with endomucin indicating a venous identity of *Apln*-expressing cells (Fig. 4c, e). Accordingly, 40% of GFP⁺ cells were observed in, or directly adjacent to, villus venules (Fig. 4c, d). The preferential expression of *Apln* in venous endothelial cells was confirmed in an independent strain of *Apln-CreERT2* mice (Extended Data Fig. 5f-h). *Aplnr* was expressed in most endothelial cells both at steady-state and during crypt expansion (Extended Data Fig. 5i).

Angiogenic tip cells in postnatal retina express APLN³¹. However, filopodia-bearing GFP⁺ESM1⁺ intestinal endothelial tip cells represented a minority of *Apln*-expressing cells, as about 70% of *Apln*-expressing cells were ESM1-negative (Fig. 4f). Consistent with low VEGFA signaling, MADCAM1⁺ villus venules, which harbored ~20% of *Apln*-expressing cells, displayed low VEGFR2 expression (Fig. 4g). We also analyzed *AplnCreERT2; mTmG* mice after DC101-mediated VEGFA signaling blockade (Extended Data Fig. 5j). Despite efficient VEGFA signaling inhibition indicated by loss of endothelial filopodia (Extended Data Fig. 2i) and decreased ESM1, APLN⁺ endothelial cells were maintained in villus vessels (Extended Data Fig. 5j), indicating that APLN expression is largely VEGFA-independent in villi. Analysis of human CRC scRNAseq data³³ indicated that *APLN* and *ESM1* were co-expressed in endothelial cells from both Wnt^{high} and Wnt^{low} tumors, however Wnt^{high} tumors harbored an additional cluster composed of endothelial cells displaying high *APLN* and low *ESM1* expression (Supplementary Fig. 3 and Supplementary Table 5). Thus, the intestinal vasculature harbors two populations of *Apln*⁺ endothelial cells: a population of venous endothelial cells with low VEGFA signaling and a smaller subset of VEGFA-responsive tip cells.

Apelin-dependent cell migration maintains crypt vessels

To determine if APLN plays a functional role, we analyzed *Apln*^{-/-} mice³⁴. Intestinal vascular density and endothelial cell proliferation were similar in WT and *Apln*-deficient mice (Fig. 5a and Extended Data Fig. 6a, b). However, we observed thinning and blind-ended blood vessels in *Apln*^{-/-} crypts, indicating vessel regression (Fig. 5a). Retracting blood vessels leave empty collagen IV⁺ sleeves that formerly encased vessels³⁵. The number of empty collagen sleeves was significantly higher in crypt, but not the villus vessels, of *Apln*-deficient mice (Fig. 5b and Extended Data Fig. 6c), suggesting that APLN specifically promotes crypt vessel patency and stability. Given that most *Apln*-GFP⁺ cells displayed a venous identity, we analyzed the venous marker endomucin expression in regressed vessels. Around 85% of vessel breaks were observed between two endomucin⁺ vessels (Extended Data Fig. 6d), suggesting APLN deficiency specifically disrupts venous capillaries. Importantly, endomucin⁺ crypt vessels also regressed during stem/progenitor cell expansion in *Apc*^{IEC}; *Apln*^{-/-} mice (Extended Data Fig. 6e-i).

The majority of *Apln*⁺ endothelial cells were found in villus vessels (Fig. 4c and Extended Data Fig. 5f), therefore it was perplexing that *Apln*^{-/-} mice displayed a loss of crypt vessel patency. Given the absence of crypt endothelial cell proliferation (Fig. 2j, k), we hypothesized that crypt vessels were replenished by migrating villus endothelial cells. We assessed endothelial cell dynamics in the intestinal vasculature by tracing *Apln*-expressing cells and their progeny in *AplnCreERT2;mTmG* mice (Fig. 5c). Short-term lineage tracing of *Apln*-GFP⁺ cells confirmed that they were mostly restricted to venous villus vessels. However, the number of crypt GFP⁺ endothelial cells tripled after a 21-day tracing window (Fig. 5d, f), indicating that a proportion of *Apln*-GFP⁺ endothelial cells migrate from the villus to the crypt at steady state. After 24hr, the majority of GFP⁺ villus venule or venule adjacent endothelial cells were found as single cells, however after 21 days only 25% remained as single cells and the rest were observed as multi-cell clusters (Extended Data Fig. 7a). In contrast, nearly all crypt GFP⁺ cells were found as single cells regardless of lineage tracing time, suggesting APLN⁺ cell proliferate in venules and migrate as single cells to crypt vessels (Extended Data Fig. 7a).

To determine whether APLN promotes crypt-ward endothelial cell migration, we performed lineage tracing in *AplnCreERT2; mTmG* male mice which are APLN-deficient as *Apln* is X-linked. In contrast to *Apln*-proficient mice, the number of crypt GFP⁺ endothelial cells did not significantly increase in *Apln*-deficient male mice after 21 days of lineage tracing (Fig. 5d, f). However, while few GFP⁺ endothelial cells were observed at the villus tip after both short- and long-term lineage tracing in *Apln*-proficient female mice, villus tip GFP⁺ cells were 8-fold more abundant in *Apln*-deficient male mice (Fig. 5d, g). The crypt vasculature of *Apln*^{+y} male and *Apln*^{+/-} female mice was similar to that of wild-type mice, and crypt defects were observed in both female and male *Apln*^{-/-} mice, ruling out sex-specific differences (Extended Data Fig. 7b). These results show that *Apln* is required for endothelial cell migration towards intestinal crypt vessels at steady state.

We hypothesized that endothelial cell crypt-ward migration would be enhanced during acute crypt expansion in *Apc*^{IEC} mice, correlating with increased *Apln* expression. We thus performed lineage tracing experiments after treatment with the Wnt signaling agonist

R-spondin 1 (Rspo1-Fc; Fig. 5c and Extended Data Fig. 7c)^{36,37}. Around 12% of GFP⁺ endothelial cells were observed in crypts after 3 weeks of lineage tracing in steady state *AplnCreERT2; mTmG* mice, whereas almost 20% of GFP⁺ endothelial cells were observed in crypts after just 4 days of expansion (Fig. 5d-f), indicating that rapid progenitor cell expansion increases endothelial cell migration to the crypts. Accordingly, the number of crypt GFP⁺ endothelial cells in *Apln*-deficient male *AplnCreERT2; mTmG* mice during Rspo1-Fc-mediated crypt expansion was similar to that observed after 3 weeks of lineage tracing at steady-state (Fig. 5d-f). In addition, the number of villus tip GFP⁺ endothelial cells were significantly higher in *Apln*-deficient than *Apln*-proficient mice during Rspo1-Fc-mediated crypt expansion (Fig. 5e, g). Together, these data indicate that APLN promotes villus endothelial cell migration towards the crypts, which is essential for maintaining crypt vessel patency (Extended Data Fig. 7d).

Apelin promotes crypt perfusion and progenitor maintenance

Our observation of decreased crypt vessel patency and perfusion in *Apln*^{-/-} mice prompted us to characterize intestinal stem/progenitor function. Both *Apln*^{-/-} villi and crypts were significantly smaller than controls (Extended Data Fig. 8a, b). We hypothesized decreased stem/progenitor proliferation could account for this and found significantly reduced crypt epithelial cell proliferation in *Apln*^{-/-} mice as determined by both EdU incorporation and staining for Ki67 (Fig. 6a and Extended Data Fig. 8c). Further EdU pulse-chase experiments revealed reduced epithelial cell migration in the absence of APLN (Extended Data Fig. 8d).

To determine if APLN deficiency affected crypt epithelial cell fitness, we analyzed genotoxic stress by quantifying a DNA double-strand break marker phospho- γ H2A.X. As expected³⁸, low-level phospho- γ H2A.X was detected in proliferating EdU⁺ progenitors. Intriguingly, we found that phospho- γ H2A.X⁺ EdU^{neg} crypt epithelial cells were 4 times more abundant in *Apln*^{-/-} than WT mice (Extended Data Fig. 8e). We also observed polarization of EdU⁺ cells to one side of the crypt in *Apln*^{-/-} mice after both acute and pulse-chase EdU injections; conversely, EdU⁺ cells were more evenly distributed in WT mice, suggesting that decreased cell proliferation in *Apln*^{-/-} mice occurred in discrete crypt zones (Fig. 6a and Extended Data Fig. 8d, f-h). Indeed, 3D reconstruction of crypt epithelial cells and associated vessels showed a lack of EdU incorporation near regressed vessels (Fig. 6b). Loss of vessel patency also affected crypt perfusion as intravenous injection of fluorescently labeled PECAM1 antibodies showed numerous non-perfused crypt vessels in *Apln*^{-/-} mice (Extended Data Fig. 8i). Furthermore, accumulation of i.v.-injected cell-permeable nuclear dye Hoechst 33342 was significantly lower around occluded crypt vessels in *Apln*^{-/-} mice, compared to patent crypt vessels in control mice (Fig. 6c), demonstrating *Apln*-deficiency results in reduced crypt perfusion and decreased stem/progenitor cell proliferation and maintenance.

Endothelial APLN could signal directly to intestinal epithelial cells, however expression of *Aplnr* was undetectable in either EPCAM⁺CD44⁺ stem/progenitor or EPCAM⁺CD44^{neg} differentiated epithelial cells (Extended Data Fig. 8j, k). Fewer organoids grew from *Apln*^{-/-} than *Apln*^{+/+} crypt epithelial cells directly after harvest, consistent with the observation of smaller crypts in *Apln*^{-/-} mice. However, control and *Apln*^{-/-} intestinal organoids grew at

equal rates after replating (Extended Data Fig. 8l, m), showing that defects in *Apln*^{-/-} crypt epithelial cell maintenance and proliferation are cell-extrinsic.

To determine the epithelial cell subset affected by APLN deficiency we sorted CD44⁺ crypt epithelial cells from wild-type and *Apln*^{-/-} mice and analyzed their transcriptomes by RNAseq (Extended Data Fig. 8j). While expression of canonical and reserve stem cell markers was not significantly changed, secretory progenitor markers (*Atoh1*, *Dll1*, *Prox1*)¹ were downregulated, as was expression of the proliferation marker *Mki67* (Fig. 6d), consistent with decreased proliferation in *Apln*^{-/-} crypt epithelial cells (Fig. 6a and Extended Data Fig. 8c). Tuft and enteroendocrine (EE) cell marker genes (*Dclk1*, *Trpm5*, *Pou2f3*, *Chga*) were also downregulated in *Apln*^{-/-} crypt epithelial cells (Fig. 6d). We deconvoluted our bulk RNAseq data using a scRNAseq-derived transcriptional signature of *Prox1*⁺, *Bmi1*⁺ and *Lgr5*⁺ epithelial cells³⁹. This analysis confirmed that genes downregulated in *Apln*^{-/-} crypts were enriched in the secretory progenitor cluster, but also in tuft and EE clusters (Extended Data Fig. 9a-c). Expression of stem and Paneth cell genes were increased in *Apln*^{-/-} crypt epithelial cells (Extended Data Fig. 9a, b), however, this was likely due to the increased ratio of stem/Paneth cells owing to loss of other crypt cells. Accordingly, we did not observe an increase of *Lgr5*-GFP⁺ crypt-based columnar stem cells in *Apln*^{-/-}; *Lgr5*-GFP-CreERT2 mice (Extended Data Fig. 9d). Secretory progenitors, in particular a PROX1⁺ population with a mixed EE/tuft phenotype, display injury-induced stem cell activity, and inducible depletion of DCLK1-expressing tuft-like cells reduced growth of human colon cancer xenografts³⁹⁻⁴¹, therefore we stained for PROX1, DCLK1 and the EE marker CHGA in *Apln*^{-/-} mice. We found that the numbers of crypt DCLK1⁺PROX1⁺ and CHGA⁺ cells were significantly decreased in *Apln*^{-/-} crypts, whereas the numbers of villus DCLK1⁺ and CHGA⁺ cells were unchanged (Fig. 6e and Extended Data Fig. 9e, f), suggesting a loss of injury-inducible DCLK1⁺PROX1⁺ progenitors in *Apln*^{-/-} mice.

We found that O₂-consuming metabolic pathways were enriched in human Wnt^{high} CRC tumors (Fig. 1d). To determine if this is recapitulated in the absence of APLN, we performed GSEA on RNAseq data from wild-type and *Apln*^{-/-} crypts. Hallmark pathways for oxidative phosphorylation, peroxisomes and MYC signaling, associated with Wnt^{high} CRC tumors (Fig. 1d), were lost in *Apln*^{-/-} crypt epithelial cells (Fig. 6f). Collectively, these results suggest that APLN-dependent crypt vessel patency is necessary to maintain niche perfusion and essential for injury-inducible progenitor cell maintenance (Fig. 6g).

APLN promotes progenitor cell normoxia and CRC growth

We next assessed the impact of *Apln* deficiency during pathological stem/progenitor cell expansion. Loss of vessel patency was observed in *Apc*^{IEC}; *Apln*^{-/-} mice (Extended Data Fig. 6g, h), therefore we analyzed crypt epithelial cells in these mice. *Apc*^{IEC}; *Apln*^{-/-} mice displayed significantly reduced crypt epithelial cell expansion and proliferation (Extended Data Fig. 10a-d). Furthermore, EdU^{neg}, phospho-γH2A.X⁺ progenitors were significantly increased in *Apc*^{IEC}; *Apln*^{-/-} compared to *Apc*^{IEC} mice (Extended Data Fig. 10e), while the number of crypt PROX1⁺ and DCLK1⁺ cells were significantly decreased (Fig. 7a), indicating that APLN promotes transformed progenitor cell expansion and maintenance. Importantly, the number of HIF1α⁺ hypoxic crypt epithelial cells was significantly increased

in *Apc*^{IEC}; *Apln*^{-/-} compared to *Apc*^{IEC} mice (Fig. 7b), indicating that APLN promotes crypt vessel stability ensuring progenitor cell normoxia during expansion.

We next investigated the role of APLN in CRC tumor growth. Orthotopically-injected AKP organoid tumors grew significantly less in *Apln*^{-/-} mice than controls (Fig. 7c). To assess the impact of APLN on tumor initiation, we generated *Apc*^{fl/+}; *Vil-CreERT2* and *Apc*^{fl/+}; *Vil-CreERT2*; *Apln*^{-/-} mice, administered tamoxifen and dissected tumors after 80 days (Fig. 7d). The control mice harbored an equal number of small (<2-3mm) and big (>3mm) tumors, while 80% of tumors in *Apc*^{fl/+}; *Vil-CreERT2*; *Apln*^{-/-} mice were small (Fig. 7e-g). APLN is therefore dispensable for tumor initiation but needed for expansion of Wnt^{high} adenomas and CRCs.

Apln-deficiency also significantly inhibited growth subcutaneously implanted AKP organoids (Fig. 7h, i). Numbers of CD44⁺ and PROX1⁺ progenitor, but not *Lgr5*⁺ stem cells, were markedly reduced in *Apln*^{-/-} mice showing that APLN supports progenitor but not LGR5⁺ stem cell populations in tumors (Fig. 7j, k and Extended Data Fig. 10f). In line with observations in normal intestinal crypts (Fig. 6e and Extended Data Fig. 9e), we also observed fewer DCLK1⁺/PROX1⁺ cell in *Apln*^{-/-} AKP tumors (Fig. 7l and Extended Data Fig. 10g). Vessel density was significantly decreased in PROX1⁺ cell areas, whereas vascular density in PROX1^{neg} zones remained unchanged (Extended Data Fig. 10h) and CD44⁺ progenitor cells in AKP tumors were more hypoxic in *Apln*^{-/-} mice than WT mice (Fig. 7m). Collectively, these results suggest that APLN maintains progenitor-associated vessels, which sustain both rare DCLK1⁺/PROX1⁺ injury-inducible³⁹ and more numerous DCLK1⁻/PROX1⁺^{11,12} cancer progenitor cells and in turn promote tumor growth.

To test whether APLN is sufficient to improve tumor vessel functionality, we stably overexpressed APLN in MC38 cells, whose growth is sensitive to VEGFA-blockade (Extended Data Fig. 4c and Supplementary Fig. 4a, b). APLN overexpression did not affect MC38 cell growth *in vitro* (Supplementary Fig. 4c). Therefore, we treated mice carrying established MC38-GFP and MC38-APLN subcutaneous tumors with control IgGs or DC101. DC101 significantly inhibited MC38-GFP tumor growth (Supplementary Fig. 4d) and decreased vascular density, endothelial cell proliferation, ESM1 expression, and cancer cell proliferation (Supplementary Fig. 4f-k). Overexpression of APLN reduced tumor growth and rendered them insensitive to VEGFR2 signaling blockade (Supplementary Fig. 4e), as DC101 had no effect on vascular density and on endothelial or cancer cell proliferation in MC38-APLN tumors (Supplementary Fig. 4f, g, i). Furthermore, significantly more vessels were covered with α SMA⁺ mural cells in MC38-APLN tumors, regardless of DC101 treatment, demonstrating that APLN promotes blood vessel maturation and stability (Supplementary Fig. 4j, l). Lastly, the number of HIF1 α ⁺ cells was significantly reduced in MC38-APLN compared to MC38-GFP tumors, even in DC101-treated mice (Supplementary Fig. 4m). These results indicate that local APLN expression is sufficient to promote the formation of a perfused, quiescent, and VEGFA-independent vascular network.

Discussion

Here we show that Wnt-driven intestinal progenitor cell expansion promotes blood vessel growth in a VEGFA-independent fashion. Rather, endothelial APLN expression is induced, promoting venous endothelial cell migration towards the stem/progenitor cell zone, thereby stabilizing crypt vessels and preventing hypoxia. We propose that the requirement for maintaining normoxia is due to the preferential use of O₂-dependent metabolism by transformed stem/progenitor cells during pathological expansion. APLN deficiency induces crypt hypoxia and reduces proliferation and survival of intestinal progenitor cells. Thus, our study puts forward a model whereby APLN signaling maintains blood vessel patency to promote non-sprouting vascular expansion during pathological progenitor cell growth.

It may seem paradoxical that normal and Wnt^{high} CRC progenitors expand a vessel network in a VEGFA-independent manner. However, we observed that progenitor niches are invariably normoxic compared to differentiated cell niches; accordingly, VEGFA signaling blockade inhibited neither progenitor cell nor vessel expansion. We propose that unlike sprouting angiogenesis a “filling-in” mechanism expands preexisting functional tumor vasculature, which prevents the onset of hypoxic conditions. Wnt^{high} CRC primarily use O₂-dependent metabolism, therefore, selective pressure to maintain normoxia is likely driving this unusual vessel expansion. A non-angiogenic “replacement” growth pattern was observed in VEGFA blockade-resistant CRC liver metastases⁴². These observations are consistent with our data showing Wnt^{high} CRC-mediated vessel normalization and we hypothesize the replacement growth pattern could be a feature of Wnt^{high} tumors. While many normal stem cells rely on hypoxia to remain in an undifferentiated state⁴³, stem cells from several cancers rely on metabolic adaptation and oxidative phosphorylation⁴⁴. The direct Wnt target PROX1 promotes oxidative phosphorylation and metabolic adaptation of CRC cells¹¹ which are necessary for normal and CRC progenitor maintenance⁴⁵ and PROX1⁺ cells are specifically maintained by APLN-mediated vessel remodeling.

Mechanistically, we show that APLN promotes crypt-ward endothelial cell migration resulting in the maintenance of blood vessel patency during progenitor cell expansion-induced vessel growth. Our results reinforce the notion that endothelial cell migration is a major mechanism contributing to development and expansion of vascular networks^{46–48} and highlight the therapeutic potential of targeting such migration in pathological conditions. APLN expression is promoted by VEGFA and hypoxia in other tumor types and during development^{49–54}. However, in our model APLN expression was largely VEGF-independent, indicating the existence of additional mechanisms. Importantly, consistent with our results *APLN* is preferentially expressed in tumor endothelial cells from bevacizumab-resistant CRC and ovarian cancer patients^{55,56} and is induced in mouse tumors following anti-angiogenic treatment⁵⁷. Recently it was reported that APLN suppression in breast cancer cells decreased tumor hypoxia⁵⁴. However, we found that AKP tumors had severely decreased growth and increased progenitor cell hypoxia when implanted in *Apln*^{-/-} mice and APLN overexpression in MC38 tumor cells decreased hypoxia, coincident with increased pericyte coverage. These results are consistent with previous work showing that, by promoting blood vessel patency, APLN acts as a pro-normoxia factor^{29,31}.

Acute crypt expansion doubles the size of the progenitor cell niche in as few as 6 days. Thus, the underlying stromal cells must cope with rapid tissue expansion. Accordingly, *Apln*^{-/-} mice display decreased endothelial cell migration upon crypt expansion resulting in regression of crypt vessels. Vessel regression was mostly limited to crypt endomucin⁺ venous capillaries. In other organs APLN signaling has also been shown to be necessary for venous vessel stability^{26,31,58}. APLNR signaling promotes biomechanical responses in endothelial cells⁵⁹, therefore, APLN/APLNR signaling may be a general venous response to biomechanical forces to ensure maintenance of vessel patency. We observed VEGFA-independent *Apln* expression and many APLN⁺ endothelial cells on VEGFR2-low venules and speculate that this population serves as reserve cellular pool to adjust to mechanical stress. Apelin therefore could be a major pathway driving venous to arterial intravessel migration as described in other contexts^{46-48,60}. Our data that APLN-expressing endothelial cells maintain intestinal progenitor cells broadly agree with the role of apelin⁺endomucin⁺ endothelial cells in hematopoietic stem cell maintenance and expansion after radiation treatment²⁸, albeit via distinct mechanisms.

Our results have uncovered the selective sensitivity of crypt epithelial cells to vascular disruption. We found that numbers of crypt DCLK1⁺ and CHGA⁺ cells but not LGR5⁺ columnar stem cells were significantly decreased in *Apln*^{-/-} crypts, consistent with the loss of injury-inducible progenitors. At steady-state PROX1 is a marker of these progenitors³⁹ and crypt Wnt-driven crypt expansion greatly expands the number of PROX1⁺ cells which are essential for Wnt^{high} tumor growth^{11-13,25}. Interestingly, PROX1⁺ injury-inducible progenitors are present in a mosaic fashion in the normal intestine, but their numbers are greatly expanded after injury³⁹. Here we hypothesize that Wnt-driven crypt transformation co-opts the injury-inducible response and APLN-mediated crypt vessel maintenance and resulting perfusion is necessary to support this essential for tumor growth population.

In conclusion, we show that endothelial APLN signaling contributes to maintaining the intestinal progenitor cell niche both at steady state and in cancer and present a mechanistic rationale for the intrinsic resistance of CRC progenitor cells to VEGFA blockade. These results put forward the notion that organotypic features of vasculature, reflecting cancer origin, contribute to treatment resistance and that targeting APLN and endothelial cell migration may represent a strategy for treating Wnt^{high} CRC.

Methods

Mouse models

All animal experiments were approved by the Animal Ethics Committee of Vaud, Switzerland. *Apc*^{fl/fl}, *p53*^{fl/fl}, *Kras*^{G12D}, *Apc*^{min/+}, *Apln*^{-/-}, *Kdr*^{fl/fl}, *Cdh5-CreERT2*, *Prox1*^{fl/fl}, *Apln-CreERT2*, *mTmG*, *Lgr5-EGFP-CreERT2* and *Vil-CreERT2* mice were previously described^{32,34,61-70}. *Apln-HA-NLS-Phimut-2A-iCreERT2* mice (Fig. S9F-H) were provided by Dr. Rui Benedito. All mice were maintained on a C57Bl/6 background except for *Apln-CreERT2* and *Apln-HA-NLS-Phimut-2A-iCreERT2* which were on a C57Bl/6-C3H mixed background. Experiments were performed with age and sex-matched cohorts of 8–12-week-old mice (unless otherwise noted) and consisted of males and females in approximately equal numbers. Mice were provided water and food (Scientific Animal

Food & Engineering, R150) ad libitum. Mice were on a 12 hour light/dark cycle and kept at $22^{\circ}\text{C}\pm 2^{\circ}\text{C}$ with relative humidity of $55\%\pm 10\%$. Cre-mediated deletion was induced in 8 mice either by intraperitoneal (i.p., 50mg/kg mouse) or subcutaneous injection (100mg/kg mouse) of tamoxifen in sunflower oil (Sigma). For *Apln-CreERT2; mTmG* experiments 4-OHT (Sigma, 50mg/kg) was injected i.p. 24 hours or 3 weeks before dissection. We did not observe any effects of tamoxifen injection on Cre-negative animals. The blocking antibody DC101, which blocks the interaction of ligands with VEGFR2, was described previously¹⁹. Anti-VEGFR2 and control rat anti-horseradish peroxidase IgG (BioXCell) were delivered by i.p. injections (40 mg/kg mouse) every 3 days for up to 14 days. Pimonidazole (60mg/kg mouse; Hypoxyprobe) was injected i.p. 1 hour or 30 min. prior to sacrifice. EdU (10mg/kg mouse; Invitrogen) was injected 30 min. prior to sacrifice, except for pulse/chase experiments where it was injected i.p. 72h before dissection. Mouse RSPO1-Fc was produced by the Protein Expression Core Facility (EPFL, Lausanne) and injected i.p. (4.5mg/kg mouse). For vessel perfusion assays 30 μ l PE-conjugated PECAM1 antibody (eBioscience, clone 390) or Hoechst 33342 (100 μ l, 3.5mg/ml) was injected i.v. 5 min. prior to sacrifice.

Mouse tissue collection, staining procedures and image acquisition

For intestinal whole-mount immunostaining⁷¹ mice were perfusion fixed and the intestine was dissected and fixed overnight in fixation buffer (0.5 % PFA, 15% picric acid, 1X PBS). After washing in 1X PBS, intestinal pieces were incubated with primary and secondary antibodies overnight, with washing all day after staining (0.3% Triton-X100, 1X PBS). After the last wash, samples were post-fixed with 4% PFA, 1X PBS overnight. All steps were performed at 4°C. The next day, samples were cleared in RIMS buffer⁷² and mounted for imaging. For paraffin sections, mice were perfusion fixed and tissues were dissected and fixed overnight (4% PFA, 1X PBS). Samples were washed and embedded in paraffin. After sectioning, samples were deparaffinized, rehydrated and antigen retrieval was performed with either Tris- or Citrate-based Antigen Unmasking Solution (Vector Labs). Samples were incubated with primary antibodies overnight at 4°C and washed with 0.3% Triton-X100, 1X PBS. Secondary antibody incubation was performed for 1hr at room temperature and followed by washing and mounting. Primary antibodies are listed in Supplementary Table 6 and were resuspended according to manufacturers' recommendations when supplied lyophilized. Alexa Fluor 488, 555, and 647 fluorochrome-conjugated secondary antibodies (Invitrogen) were used for signal detection. Nuclei were detected with DAPI. Confocal images were obtained using Zeiss LSM 780, Zeiss LSM 510 META or Leica SP5 TANDEM microscopes and standard fluorescent images were obtained using a Zeiss Axio Imager Z1. Images were analyzed using Zen (Zeiss), Imaris (Bitplane), ImageJ (NIH) and Photoshop (Adobe) software.

RNAscope fluorescent in situ hybridization

RNAscope Multiplex Fluorescent V2 assay (Bio-technne) was performed according to manufacturer's protocol on 4 μ m paraffin sections, hybridized with probes Mm-Apln (Bio-technne, Cat. No. 415371), Mm-Aplnr (Bio-technne, Cat. No. 436171) or Mm-Lgr5-C2 (Bio-technne, Cat. No. 312171-C2) at 40°C for 2 hours and revealed with TSA Opal570 (1:1500,

Perkin Elmer). Tissues were counterstained with DAPI and mounted with ProLong Gold (Thermo Fisher).

Human tissue collection, staining procedures and image acquisition

Formalin-fixed paraffin embedded human colon cancer with matched normal tissue samples were obtained from the Institute of Pathology Biobank (CHUV, Lausanne, Switzerland) and approved by the Commission d'Éthique du Canton de Vaud under project number 2016/057. Samples were incubated with primary antibodies overnight at 4°C and washed with 0.3% Triton-X100, 1X PBS. Secondary antibody incubation was performed for 1hr at room temperature and followed by washing and mounting. Antibodies listed in Supplementary Table 6. Bright field images were acquired using a Zeiss AxioScan Slidescanner Z1.

Cell line production, culture, treatment and implantation

To obtain intestinal organoid cultures, *Apc^{fl/fl}*; *Kras^{G12D}*; *p53^{fl/fl}*; *Villin-CreERT2* mice were injected daily with tamoxifen (50mg/kg). After 4 days, intestinal crypts were isolated and cultured in Matrigel (Corning, 356231), advanced DMEM/F12 supplemented with 1X GlutaMAX (Gibco), 10mM HEPES (Gibco), 1mM penicillin/streptomycin (Gibco) and growth factors B-27 and N-2 (Gibco), as described previously⁷³. For subcutaneous intestinal organoid implantation, organoids were dissociated, and cells were re-plated in Matrigel. After 3 days in culture, the organoids were collected from Matrigel with Cell Recovery Solution (Corning), stained with trypan blue and counted. The organoids were then resuspended in 1:1 Matrigel/Advanced DMEM/F12 and 50 organoids were injected subcutaneously with a 20G needle. AP and APP orthotopic tumors were induced by intracaecal injection of 15µl of 10mg/ml tamoxifen (Sigma), dissolved in Cremophor EL (Sigma) using an Omnican 50 syringe with 28G needle (Braun) under a stereomicroscope as described previously²⁵.

GFP and *Apln* cDNAs were inserted downstream to the spleen focus forming virus (SFFV) promoter sequence of a SFFV-OPF-WPRE lentiviral vector, described previously⁷⁴, using BamHI and SalI restriction sites. Lentiviral vectors produced in HEK-293T cells (ATCC, CRL-3216) were used to transduce MC38 cells at MOI 5-10. MC38 cells were provided by Dr. J. Schlom (NCI). The MC38 parent line, MC38-GFP, and MC38-APLN cells were injected (1x10⁶ cells in 100µl 1X PBS) subcutaneously into either NSG or C57Bl/6 mice. Control or DC101 antibodies were injected when tumors reached 200 mm³. Maximum tumor size allowed under our mouse license is 1000 mm³ and was not exceeded in this study.

ELISA

MC38-GFP and MC38-APLN cells were grown for 4 days and conditioned medium was collected. ELISA was performed using the Apelin EIA Kit (Phoenix Pharmaceuticals) according to manufacturer's instructions after diluting conditioned medium 1:2 in ELISA buffer.

Intestinal BEC sorting

8 week-old control (*Apc^{fl/fl}*) or *Apc^{fl/fl}; Vil-CreERT2* mice were injected s.c. 5 consecutive days with 10mg/ml tamoxifen. On day 6 mice were sacrificed and the intestine was dissected and flushed with ice-cold PBS. Peyer's patches were removed and the intestine was cut into 1 cm pieces, which were put in a 10mM EDTA solution agitating at 37°C for 30 min. to remove epithelial cells. The remaining tissue was then digested with Collagenase IV (3mg/mL) in complete DMEM (Gibco) containing CaCl₂ (2mM) and 50ug/ml DNase I (with constant stirring at 37°C) for 20 min and washed with medium. The cell suspension was incubated with labeled antibodies listed on Supplementary Table 6. FACS sorting was performed on a BD FACSAria IIu (BD Biosciences).

Intestinal epithelial cell sorting

C57Bl/6 and *Apln^{-/-}* mice were sacrificed and the intestine was dissected and flushed with ice-cold PBS. Peyer's patches were removed and the intestine was cut into 1 cm pieces and digested with Liberase TL (Roche) in DMEM with 2% FCS with constant stirring at 37°C for 20 min and washed with medium. The cell suspension was incubated with labeled CD31, CD44, CD45 and EpCAM antibodies listed on Supplementary Table 6. FACS sorting was performed on a BD FACSAria III (BD Biosciences) and live, CD31^{neg}CD45^{neg}EpCAM⁺ cells were sorted into CD44⁺ or CD44^{neg} fractions and collected for RNA.

RNA isolation and RT-qPCR

Total RNA was isolated using the Qiagen RNeasy Plus Micro Kit (Qiagen). Reverse transcription was performed using Transcriptor First Strand cDNA Synthesis Kit (Roche Diagnostics). Alternatively, mRNA was amplified using Ovation® Pico WTA System V2 (Nugen). Real-time qPCR analyses were performed on StepOnePlus (Applied Biosystems) using SYBR Fast PCR Master Mix (KAPA). Analysis of gene expression was carried out using the comparative Ct (Ct) method as described by the manufacturer. Sequences of PCR primers are provided in Supplementary Table 7.

Gene expression profiling

For sorted blood endothelial cells, Affymetrix Mouse Gene 2.0 ST arrays (Affymetrix) were hybridized with biotinylated target cDNA, washed and stained according to the protocol described in Affymetrix GeneChip® Expression Analysis Manual (Fluidics protocol FS450_0007). The arrays were scanned using the GeneChip® Scanner 3000 7G (Affymetrix) and raw data was extracted from the scanned images and analyzed with the Affymetrix Power Tools software package (Affymetrix). Raw microarray data (CEL files) were imported and assessed for quality control using the oligo package from Bioconductor⁷⁵. Subsequently, background subtraction, normalization, and summarization were performed using the RMA algorithm within the oligo package. Differential expression analysis was performed using the limma package from Bioconductor⁷⁶, with LOG₂(FoldChange)=1 and Benjamini and Hochberg's adjusted-Pval=0.05 as cutoff values. Genes were ranked based on fold-change expression in *Apc^{fl/fl}; Vil-CreERT2* vs *Apc^{fl/fl}* (KO vs. WT) BECs.

For crypt intestinal epithelial cells, RNA-seq libraries were prepared from 100 ng of total RNA using the Nextera DNA Flex Kit (Illumina) using manufacturer's recommendations. Sequencing libraries were validated on the Agilent TapeStation (Agilent Technologies) and quantified by using Qubit 2.0 Fluorometer (Invitrogen) as well as by quantitative PCR. The samples were sequenced on a HiSeq 4000 SR (Illumina) with 2x150 single-end reads. Image analysis and base calling were conducted by the HiSeq Control Software (HCS). Raw sequence data (.bcl files) generated from Illumina HiSeq was converted into fastq files and de-multiplexed using Illumina's bcl2fastq 2.17 software. One mismatch was allowed for index sequence identification. We used STAR version 2.6.1⁷⁷ to map the reads to the mm10 mouse reference genome. We obtained the read counts for each reference transcripts with htseq-count⁷⁸. Differential expression analysis between KO and WT samples was performed with DESeq2⁷⁹, using standard normalization procedures. Functional analysis was done using GSEA and the log fold change of expression as a ranking metric and the molecular signatures database version 7.2.1^{80,81}.

Bioinformatics

Gene expression data and CMS calls from 2,275 CRC patients were taken from 13 public independent datasets as previously reported (Supplementary Table 1)⁵, <https://www.synapse.org/#!Synapse:syn2623706/wiki/67246>. In each dataset, the CRC patients were classified as Wnt^{high} (Wnt expression signature higher than the 80th percentile) and Wnt^{low} (Wnt expression signature lower than the 20th percentile). Patients with an intermediate expression of the Wnt expression signature were filtered out for all analyses except for comparing signature score according to CMS subtypes. To compute gene signature score for the whole cohort, gene expression data were first scaled and zero-centered independently per dataset before being merged at the gene level. The Wnt signature score is defined as the average expression of five genes (ASCL2, AXIN2, APCDD1, LGR5 and RNF43) and the Masiero signature is defined as the average expression of 43 genes reported as the core signature in Table S2 of Masiero et al.⁸².

Unbiased pathway analyses were performed with the single sample GSEA (ssGSEA) using the GenePattern web interface of the Broad Institute (<http://www.genepattern.broadinstitute.org/>). We used the Hallmark and the KEGG collections of the MSigDB portal (<http://www.broadinstitute.org/gsea/msigdb>). Enrichment scores from ssGSEA were then scaled, zero-centered per dataset and subjected to differential analysis (Wnt^{high} versus Wnt^{low}) using the regularized linear model as implemented in the *limma* package (version 3.24.4). These ssGSEA scores are presented in heatmaps created with the *heatmap* package. For correlation analysis, Pearson correlation test were performed.

Data analysis pipeline for human CRC single cell RNA sequencing data

Gene expression data and annotation for cells from 23 patients in 23 primary colorectal cancer and 10 matched normal mucosa were retrieved from NCBI geo repository GSE132465³³. The CRC patients were classified as Wnt^{high} (Wnt expression signature higher than the 80th percentile) and Wnt^{low} (WNT expression signature lower than the 20th percentile), using a Wnt signature score computed as the average expression of five genes

(*ASCL2*, *AXIN2*, *APCDD1*, *LGR5* and *RNF43*). Patients with an intermediate expression of the Wnt signature were filtered out for the downstream analyses.

Data processing was performed with Seurat version 3.1.5⁸³ using a standard analysis pipeline. The cells were filtered according to the following criteria: >200 genes and <5,000 genes; and <25% of mitochondrial gene expression in UMI counts. The data was then normalized and scaled before performing a principal component analysis using the 2'000 genes that exhibit the highest cell-to-cell variation in expression. We used a ranking of principle components based on the percentage of variance explained by each one to determine the dimensionality of the dataset. Cell clusters were identified using the first 30 principal components and a resolution parameter of 1.5. A 2-dimensional representation of the cells and the cells clusters was obtained using the non-linear dimensional reduction technique UMAP. We generated violin plots, for the genes of interest, to visualize single cell expression distributions in each cluster. Differential expression analysis between Wnt^{high} and Wnt^{low} cells within each cluster was performed using the non-parametric Wilcoxon rank sum test.

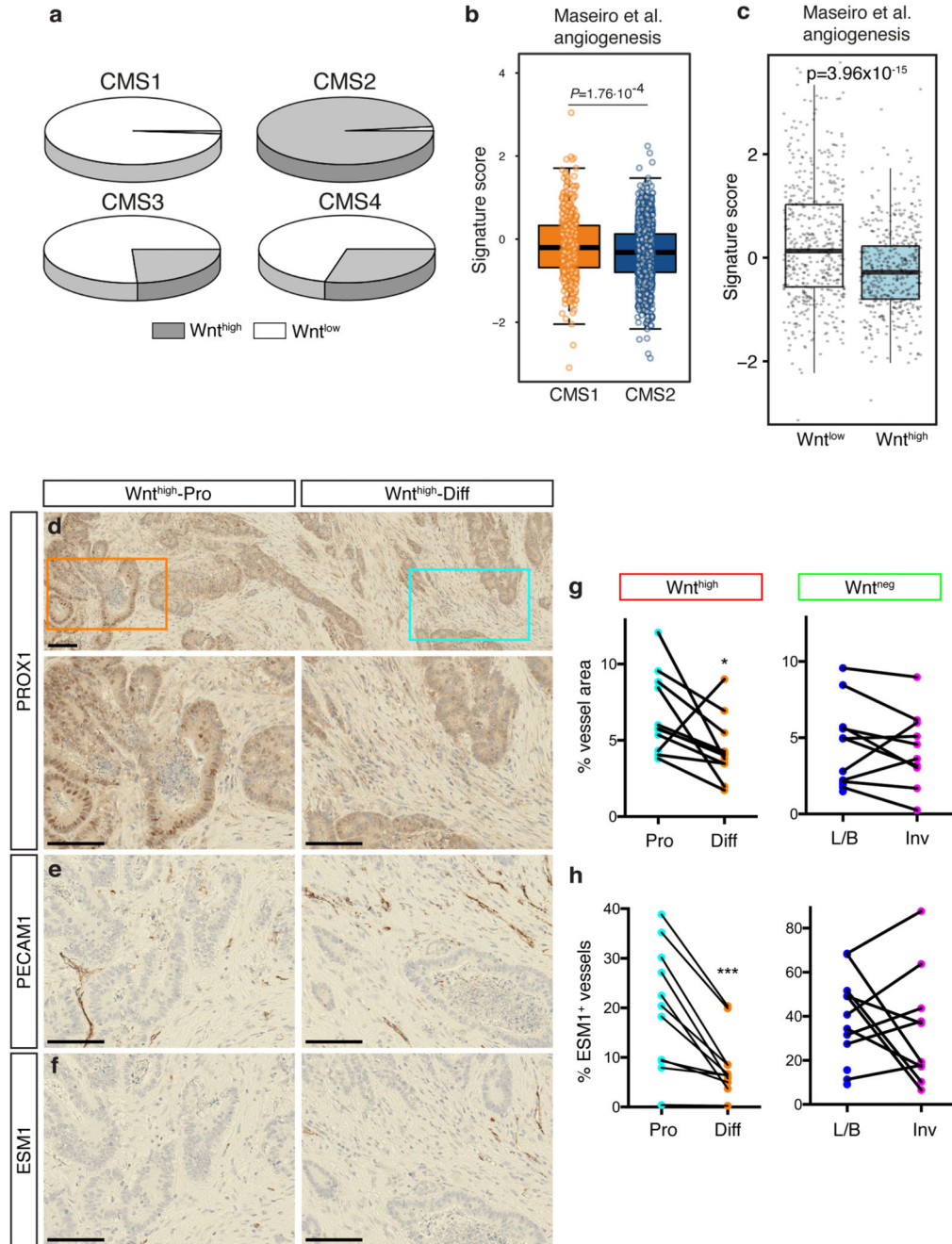
Image quantification

The cutoff between villus and crypt vessels in *Apc*^{IEC} mice was set as the bottom of the villus vessel “cage”. Villus and crypt vessel length and branching quantification were performed by drawing vessel network overlays with Photoshop and exporting these images to Angiotool⁸⁴ for quantification. For AKP organoid tumors quantification CD44^{high} areas were delineated and a 100µm-band was drawn using the “MakeBand” function in ImageJ. For cell number or vessel number, manual counting was performed. For human CRC tumor samples histopathological classification and immunostaining analysis were performed by one expert pathologist and one trainee. Both investigators were blinded to clinical data at the time of scoring. Tumor nuclear β-CATENIN and PROX1 were scored as described, with minor modifications⁸⁵. Briefly: 0, negative; 1, low, less than 20 strongly positive glands; 2, moderate, 20-40 strongly positive glands; 3, high, >40 strongly positive glands. Cancer samples were then divided into two groups according to β-CATENIN and PROX1 expression: the β-CATENIN- and PROX1-low group comprised scores of 0-1 and β-CATENIN- and PROX1-high group comprised scores of 2-3 (correlation β-CATENIN and PROX1: Pearson score $r = 0.3301$, $p = 0.0219$; inter-observer reliability: $\kappa = 0.88$ and 0.938 for β-CATENIN and PROX1, respectively). Whole tumor β-CATENIN, PROX1 and ESM1 scoring was performed as above (inter-observer reliability: $\kappa = 0.889$). Within each tumor, scoring was also performed in tumor bulk and at the invasive front. Additionally, in PROX1^{high} tumors, scoring of ESM1 was also performed in Wnt^{low} and Wnt^{high} areas to assess intra-tumor heterogeneity

Statistical analyses

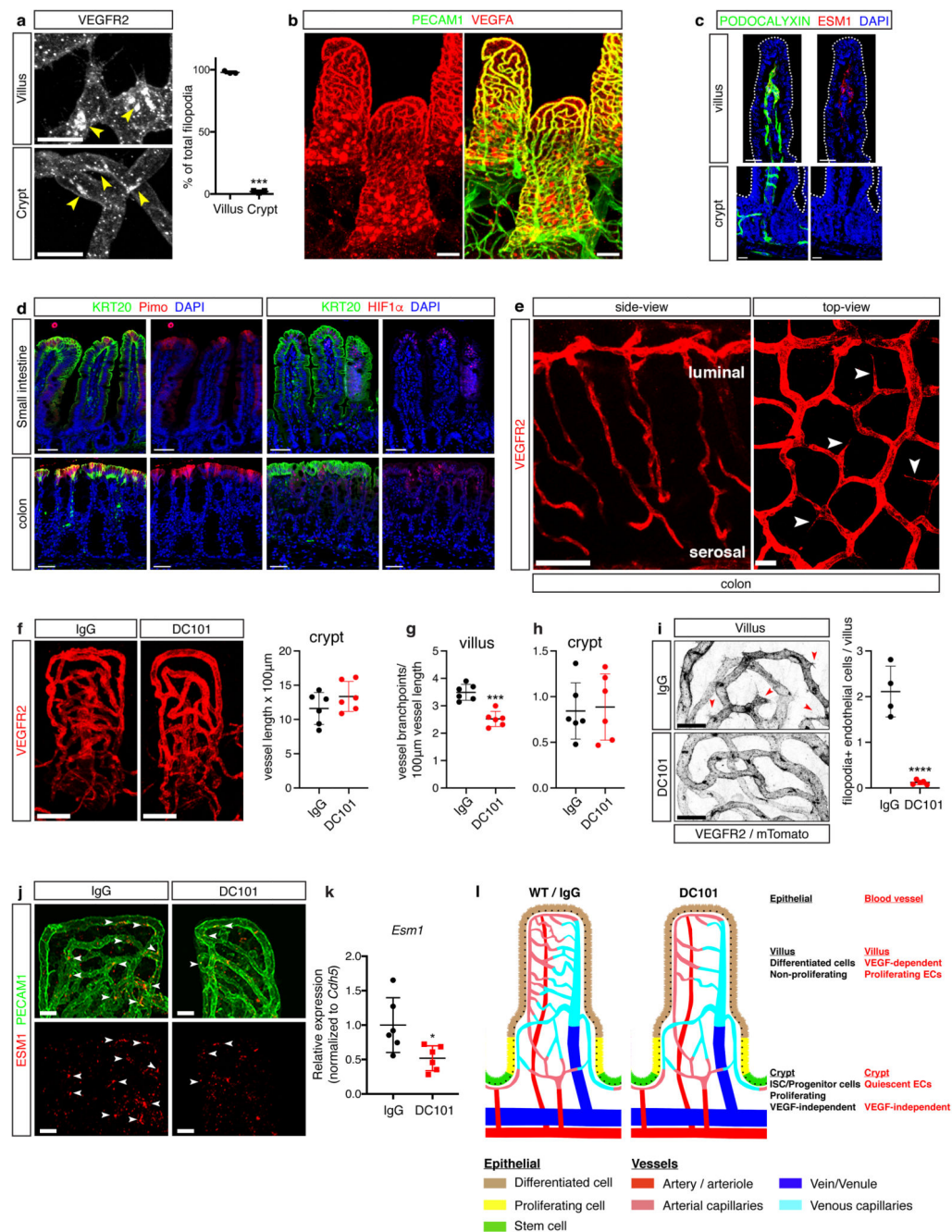
Two-tailed unpaired Student's *t* tests or one-way or two-way ANOVA were performed to determine statistical significance by calculating the probability of difference between two means, with a Bonferroni correction performed to account for multiple testing. $P < 0.05$ were considered statistically significant. Data are shown as mean ± SD.

Extended Data



Extended Data Fig. 1. Reduced VEGFA signaling near Wnt^{high} progenitors in human CRC
(a) Wnt^{high} and Wnt^{low} human CRC tumors are in CMS2 and CMS1, respectively. Distribution of CMS assignment for Wnt^{high} and Wnt^{low} human CRC tumors, $n=469$. **(b)** Angiogenic gene expression is decreased in CMS2 human CRC tumors compared to CMS1. Experimentally-derived angiogenesis signature score based on Masiero et al.¹⁰³ classified by CMS assignment, $n=2,275$. p-values from one-ANOVA with post-hoc Tukey test are

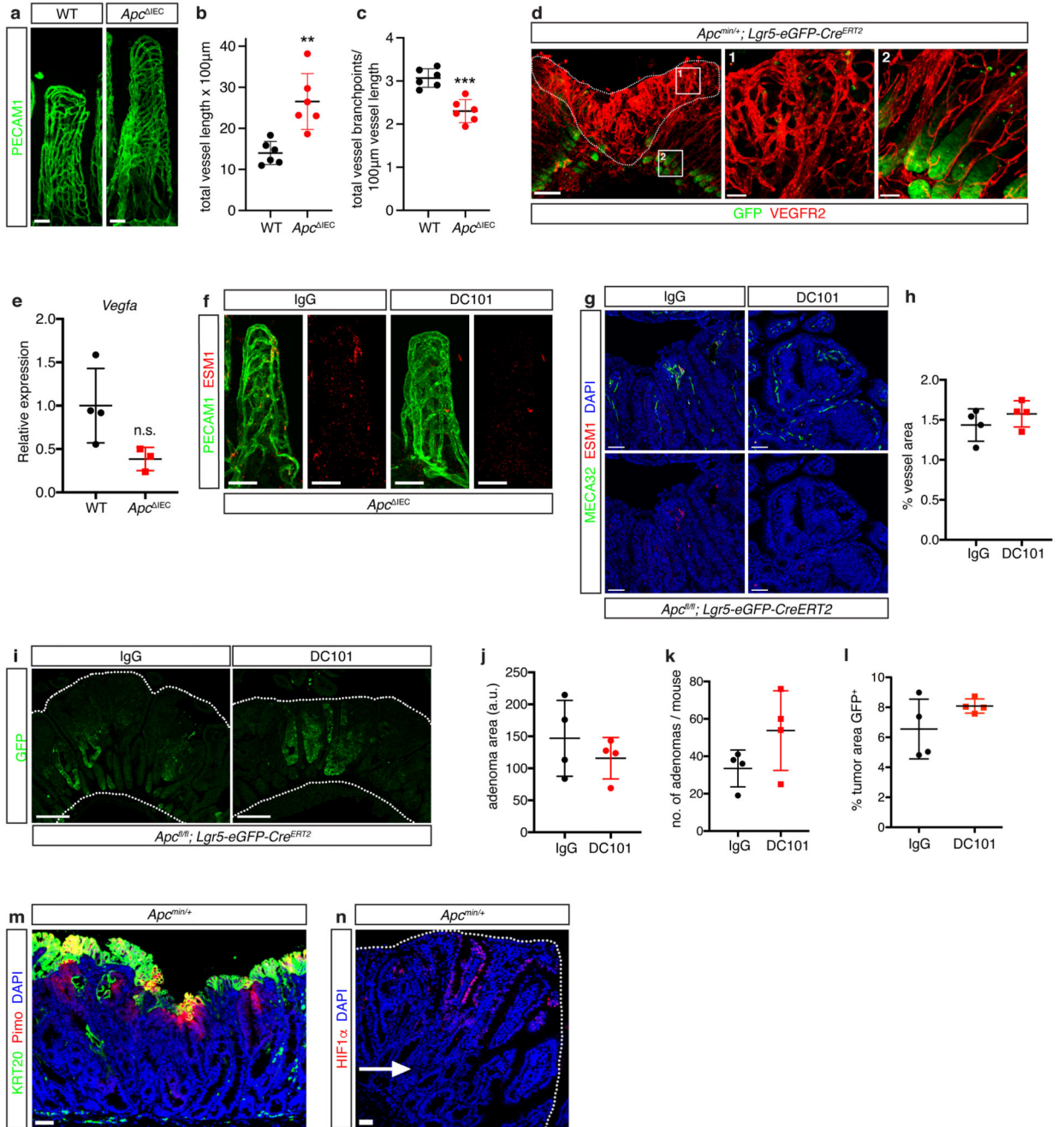
listed. **(c)** VEGF-dependent angiogenesis gene expression¹⁰³ is highest in Wnt^{low} CRC tumors, $n=469$ tumors. For boxplots, minimum (Q1) and maximum (Q3) of the box are the 25th and 75th percentile, the center is the median, the whiskers minima and maxima highlight the $Q1-1.5 \times IQR$ and $Q3+1.5 \times IQR$, where IQR is the interquartile range ($Q3-Q1$). Points outside of these regions are outliers. **(d-h)** VEGFA signaling is compartmentalized into low Wnt signaling areas of human CRC tumors. Serial paraffin section immunostaining of high (H) or low (L) areas of PROX1 staining within the same Wnt^{high} CRC tumors for **(d)** PROX1, **(e)** PECAM1 and **(f)** ESM1. **(g-h)** Quantification of percentage **(g)** vessel area (left, $p=0.0401$) or **(h)** ESM1⁺ vessels (left, $p=0.0008$) in Wnt^{high}-Progenitor (Pro) or Wnt^{high}-Differentiated (Diff) areas or luminal/bulk or invasive (L/B or Inv) areas of Wnt^{neg} CRC tumors ($n=11$ Wnt^{high} tumors and $n=8$ Wnt^{neg} tumors). Scale bars: 100 μm . All data are shown as mean \pm SD. * $P < 0.05$, *** $P < 0.001$, 2-tailed unpaired Student's t test.



Extended Data Fig. 2. Compartmentalized VEGFA in the intestinal vascular unit

(a) Filopodia are restricted to villus vessels in the intestinal vascular unit. White, VEGFR2; arrowheads indicate perinuclear VEGFR2. Quantification of the percentage of filopodia observed in villi or crypts ($p < 0.0001$, $n = 3$ mice). (b-c) VEGFA expression and signaling are restricted to the villus. (b) Whole-mount immunostaining for VEGFA (red) in adult intestinal villi is restricted to villus blood vessels (green, PECAM1). (c) ESM1 staining (red) is restricted to villus vessels (green, podocalyxin). Cryosection immunostaining, DNA (blue). (d) Crypt progenitor epithelial cells are normoxic while differentiated epithelial

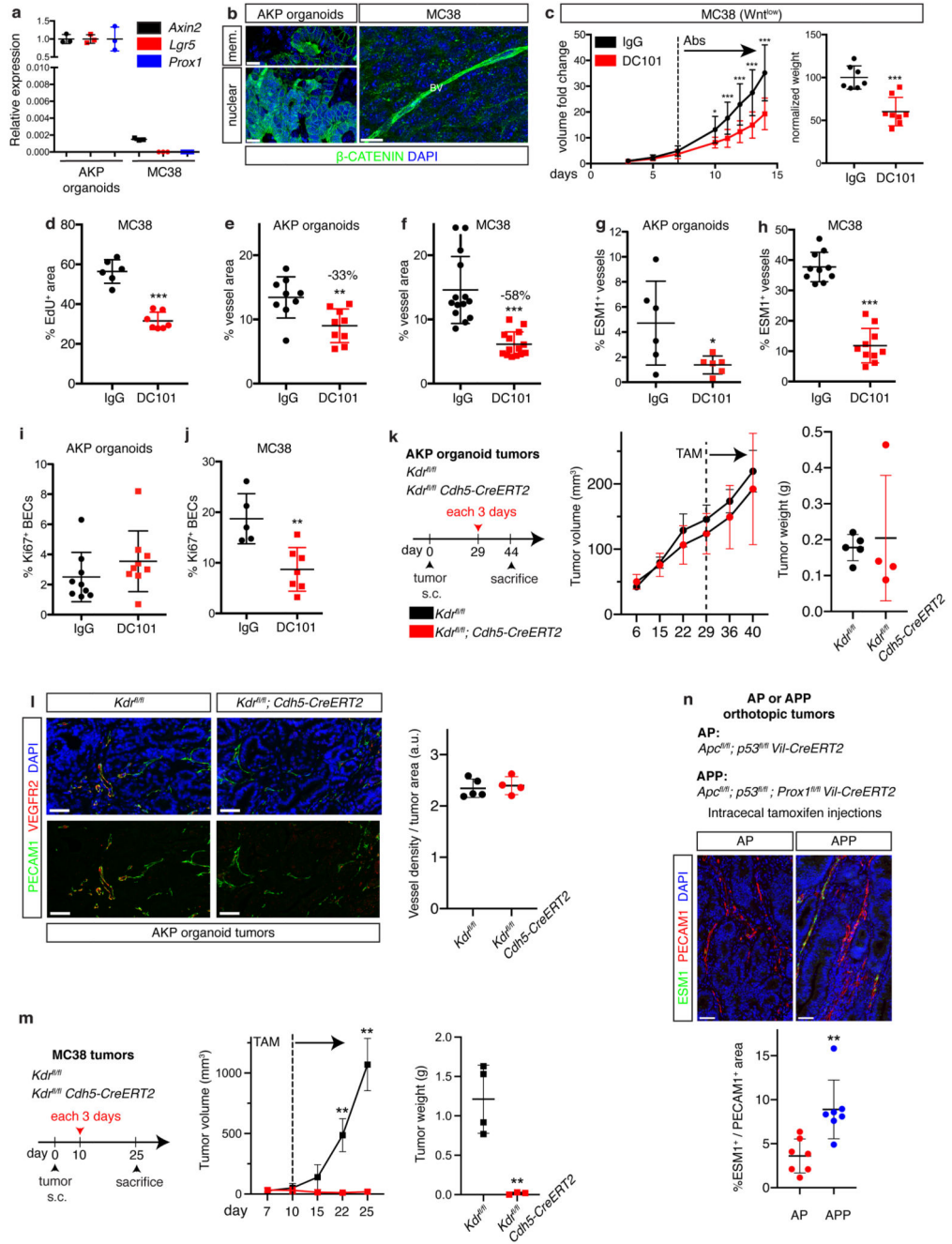
cells are hypoxic. Small intestine and colon paraffin section immunostaining for hypoxia markers pimonidazole (Pimo) and HIF1 α (red). Both hypoxia markers co-stain with the differentiated epithelial cell marker Keratin-20 (green, KRT20), DNA (blue). **(e)** Vessels associated with progenitor and differentiated colon epithelial cells are compartmentalized into normal and angiogenic vessels, respectively, as in the small intestine. Whole-mount immunostaining of colon blood capillaries (red, VEGFR2) with a side- and top-view. **(f-h)** Villus blood vessel branching is reduced in mice treated with DC101, while crypt vessel length and branching are unaffected. **(f)** Wholemout immunostaining for intestinal vessels (red, VEGFR2) and quantification of the length (x100 μ m) of crypt vessels and number of branchpoints per 100 μ m vessel length in **(g)** villus ($p=0.0002$) and **(h)** crypt vessels in mice treated with either IgG or DC101 ($n=6$ mice). **(i)** Villus vessel filopodia are dependent on active VEGFA signaling. The number of villus vessel (black, VEGFR2/mTomato) filopodia (arrowheads) is significantly reduced in mice treated with DC101. Quantification of the number of filopodia per 100 μ m of villus vessel length ($n=4$ IgG treated mice and $n=5$ DC101 treated mice; $p<0.0001$). **(j-k)** VEGFA signaling blockade decreases intestinal ESM1 expression. **(j)** Whole-mount immunostaining for ESM1 (red) on adult intestinal villi blood vessels (green, PECAM1). **(k)** Total intestine *Esm1* expression from adult control antibody- or DC101-treated C57BL/6 mice analyzed by RT-qPCR; *Esm1* expression normalized by *Cdh5* ($n=6$ mice; $p=0.0224$). **(l)** Scheme of intestinal vascular unit and VEGFA-dependence. Villus blood vessel are VEGFA-dependent and associated with differentiated epithelial cells while crypt vessels are VEGFA-independent and associated with crypt cells, including stem and proliferating progenitor cells. VEGFA blockade reduces vascular density in the villi but has no impact on crypt vessels or epithelial cell proliferation. Scale bars: 50 μ m: b, d, f; 20 μ m: a, c, e, i, j. All data are shown as mean \pm SD. * $P<0.05$, *** $P<0.001$, **** $P<0.0001$, 2-tailed unpaired Student's *t* test. Images in b-e are representative of at least 3 independent experiments.



Extended Data Fig. 3. Stem/progenitor cells are VEGFA-independent and normoxic in mouse adenomas

(a) Villus vessel length (green, PECAM1) is significantly increased in Apc^{IEC} intestine while vessel branching is decreased. (b-c) Quantification of (b) total vessel length (x100 μ m; p=0.0019) and (c) total branchpoints per 100 μ m of vessel length (p=0.0003) in control or Apc^{IEC} intestine (n=6 mice). (d) Progenitor cell expansion maintains crypt/villus vessel compartmentalization. Whole-mount immunostaining in $Apc^{min/+}; Lgr5-EGFP-CreERT2$ adenomas. Blood vessel (red, VEGFR2) density and branching is higher in the luminal

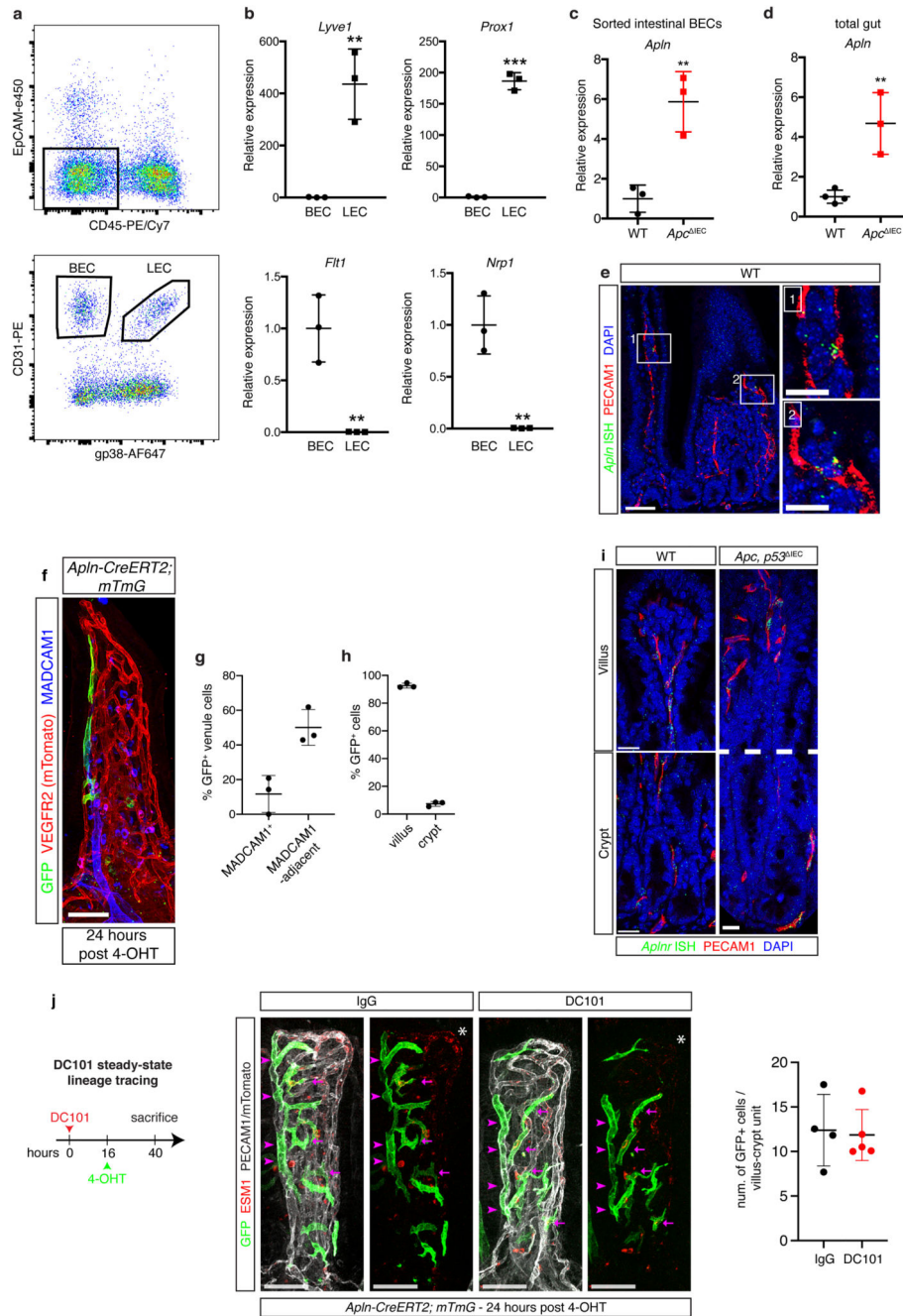
part of adenomas (Panel 1) compared to expanded epithelial crypts (Panel 2, *Lgr5*-GFP, green). Representative of 2 independent experiments. (e) VEGFA expression is not induced during progenitor expansion. qPCR for expression of *Vegfa* from total intestine of control and *Apc*^{IEC} mice, *n*=3 mice. (f-g) VEGFR2 blockade decreases ESM1 expression during progenitor expansion. (f) Whole-mount immunostaining of ESM1 (red) on villus blood vessels (green, PECAM1) in control antibody- or DC101-treated *Apc*^{IEC} mice. (g) ESM1 (red) is reduced in DC101-treated *Apc*^{fl/fl}; *Lgr5*-EGFP-*CreERT2* adenoma blood vessels (green, MECA32). Paraffin section immunostaining; DNA, blue. (h) Quantification of percentage vessel area in adenomas of control antibody or DC101-treated *Apc*^{fl/fl}; *Lgr5*-EGFP-*CreERT2* mice, *n*=4 mice. (i) Paraffin section immunostaining of GFP⁺ (green) stem cells in control antibody or DC101-treated *Apc*^{fl/fl}; *Lgr5*-EGFP-*CreERT2* adenomas (white outlines). (j-l) Quantification of control IgG or DC101-treated *Apc*^{fl/fl}; *Lgr5*-EGFP-*CreERT2* (j) adenoma area, (k) number of adenomas and (l) percentage tumor area GFP⁺, *n*=4 tumors. (m) KRT20-negative *Apc*^{min/+} adenoma crypts are Pimo-negative while differentiated KRT20⁺ lumen adjacent epithelial cells (green) are Pimo⁺ (red). (n) *Apc*^{min/+} adenoma crypt cells are HIF1 α -negative (arrow) while lumen-adjacent epithelial cells are HIF1 α ⁺ (red). Scale bars: 200 μ m: d, i; 50 μ m: a, d (insets), f, g, m, n. All data are shown as mean \pm SD, ***P* < 0.01, ****P* < 0.001, 2-tailed unpaired Student's *t* test. Images in m and n are representative of 2 independent experiments.



Extended Data Fig. 4. Stem/progenitor cells are VEGFA-independent and normoxic in models of advanced CRC

(a-b) MC38 tumor cells have low Wnt signaling. (a) qPCR for expression of Wnt target genes *Axin2*, *Lgr5* and *Prox1* in AKP organoid and MC38 tumors, $n=3$ independent samples. (b) Paraffin section immunostaining for β -CATENIN in AKP organoid and MC38 tumors. DNA, blue. (c-d) VEGFR2 blockade inhibits MC38 tumor growth and proliferation. Quantification of subcutaneous MC38 tumor organoid (c) tumor volume (left, IgG vs DC101, p value: 0.0264, day 10; 0.0093, day 11; 0.0061, day 12; 0.0046, day 13; 0.0035,

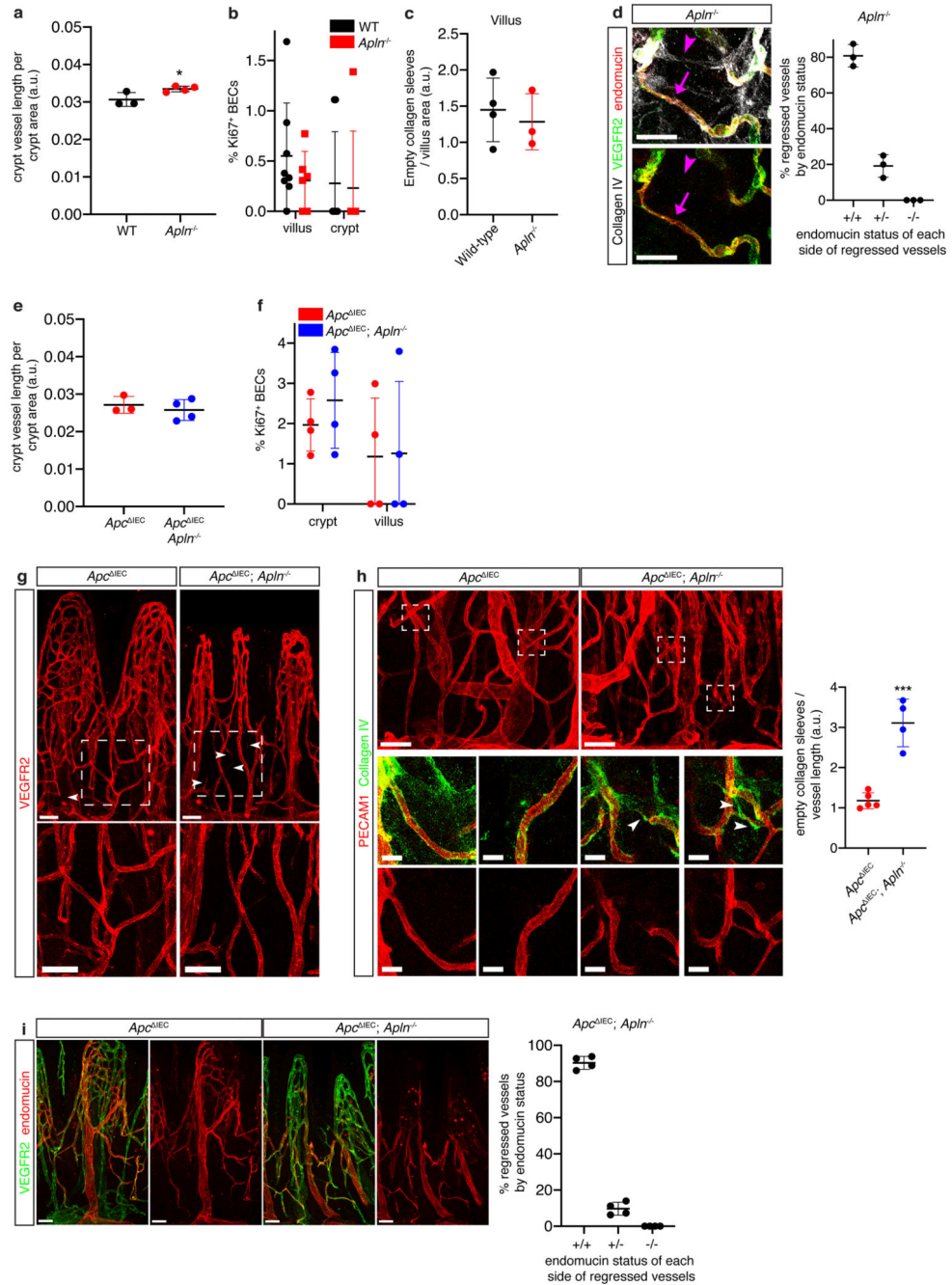
day 14) and weight (right, $p=0.0002$; $n=7$ tumors in IgG treated mice and $n=8$ tumors in DC101 treated mice). **(d)** Percentage of EdU⁺ MC38 tumor cells in control antibody- and DC101-treated mice ($p<0.0001$, $n=6$ tumors in IgG treated mice and $n=7$ tumors in DC101 treated mice, data from two independent experiments). **(e-f)** AKP organoid tumor vessels are less sensitive to VEGFR2 blockade than vessels from MC38 tumors. Quantification of tumor vessel area as a percentage of tumor area of control IgG antibody- or DC101-treated NSG mice with **(e)** AKP organoid tumors ($p=0.0056$, $n=9$ tumors) or **(f)** MC38 tumors ($p<0.0001$, $n=14$ tumors). **(g-h)** AKP organoid tumors have fewer vessels expressing the VEGF signaling-dependent ESM1 than MC38 tumors. Quantification of percentage of ESM1⁺ vessels from control antibody- or DC101-treated mice with **(g)** AKP organoid tumors ($p=0.0378$, $n=6$ tumors) or **(h)** MC38 tumors ($p<0.0001$, $n=10$ tumors). **(i-j)** AKP tumor blood endothelial cells (BECs) proliferation is resistant to VEGFR2 blockade. Quantification of % Ki67⁺ BECs from control antibody- or DC101-treated mice with **(i)** AKP organoid tumors ($n=9$ tumors) or **(j)** MC38 tumors ($p=0.0039$, $n=5$ IgG treated tumors and $n=7$ DC101 treated tumors). **(k)** Endothelial-specific ablation of VEGFR2 does not alter AKP organoid tumor growth. Experimental plan for AKP organoid tumor subcutaneous injection into *Kdr^{fl/fl}* and *Kdr^{fl/fl}; Cdh5-CreERT2* mice; tumor volume (mean \pm SEM), dotted line indicates start of tamoxifen injections $n=6$ tumors; final tumor weight (mean \pm SD, $n=5$ tumors in *Kdr^{fl/fl}* and $n=4$ tumors in *Kdr^{fl/fl}; Cdh5-CreERT2* mice). **(l)** VEGFR2 is efficiently depleted in *Kdr^{fl/fl}; Cdh5-CreERT2* mice without altering blood vessel density. Staining for PECAM1 (green), VEGFR2 (red) and DAPI (blue). Quantification of vessel density in AKP organoid tumors injected into *Kdr^{fl/fl}* and *Kdr^{fl/fl}; Cdh5-CreERT2* mice ($n=5$ tumors in *Kdr^{fl/fl}* and $n=4$ tumors in *Kdr^{fl/fl}; Cdh5-CreERT2* mice). **(m)** Endothelial-specific ablation of VEGFR2 arrests growth of MC38 tumors. Left, experimental plan for MC38 tumor subcutaneous injection into *Kdr^{fl/fl}* and *Kdr^{fl/fl}; Cdh5-CreERT2* mice. Middle, tumor volume (p value: 0.0038, day 22; 0.0011, day 25; dotted line indicates start of tamoxifen injections). Right, final tumor weight ($p=0.0055$, $n=4$ tumors in *Kdr^{fl/fl}* and $n=3$ tumors in *Kdr^{fl/fl}; Cdh5-CreERT2* mice). **(n)** Increased endothelial VEGFA signaling in tumors with decreased Wnt signaling. Staining for ESM1 (green), PECAM1 (red) and DAPI (blue). Quantification of percentage of ESM1⁺ vessels in AP and APP organoid tumor vessels ($p=0.0034$, $n=7$ tumors). Scale bars: 50 μ m: b (AKP organoids), l, n; 20 μ m: b (MC38). All data (except k, middle) shown as mean \pm SD. * $P<0.05$, ** $P<0.01$, *** $P<0.001$, 2-tailed unpaired Student's *t* test.



Extended Data Fig. 5. Confirmation of *Apln* expression in villus endothelial cells

(a) Density plots showing the gating strategy for flow cytometric sorting of intestinal blood and lymphatic endothelial cell (BEC and LEC) sorting. Single, live, CD45^{neg}, EpCAM^{neg} cells were selected (upper plot). Among those, BEC were identified and collected as CD31⁺, gp38^{neg} cells and LEC as CD31⁺, gp38⁺ cells. (b) Intestinal LEC and BEC quality control qPCR for *Flt1* ($p=0.0059$), *Nrp1* ($p=0.0036$), *Lyve1* ($p=0.0051$) and *Prox1* ($p<0.0001$, $n=3$ sorted cell samples from individual mice). (c-d) Apelin expression is induced during progenitor cell expansion. qPCR for *Apln* expression in (c) sorted intestinal

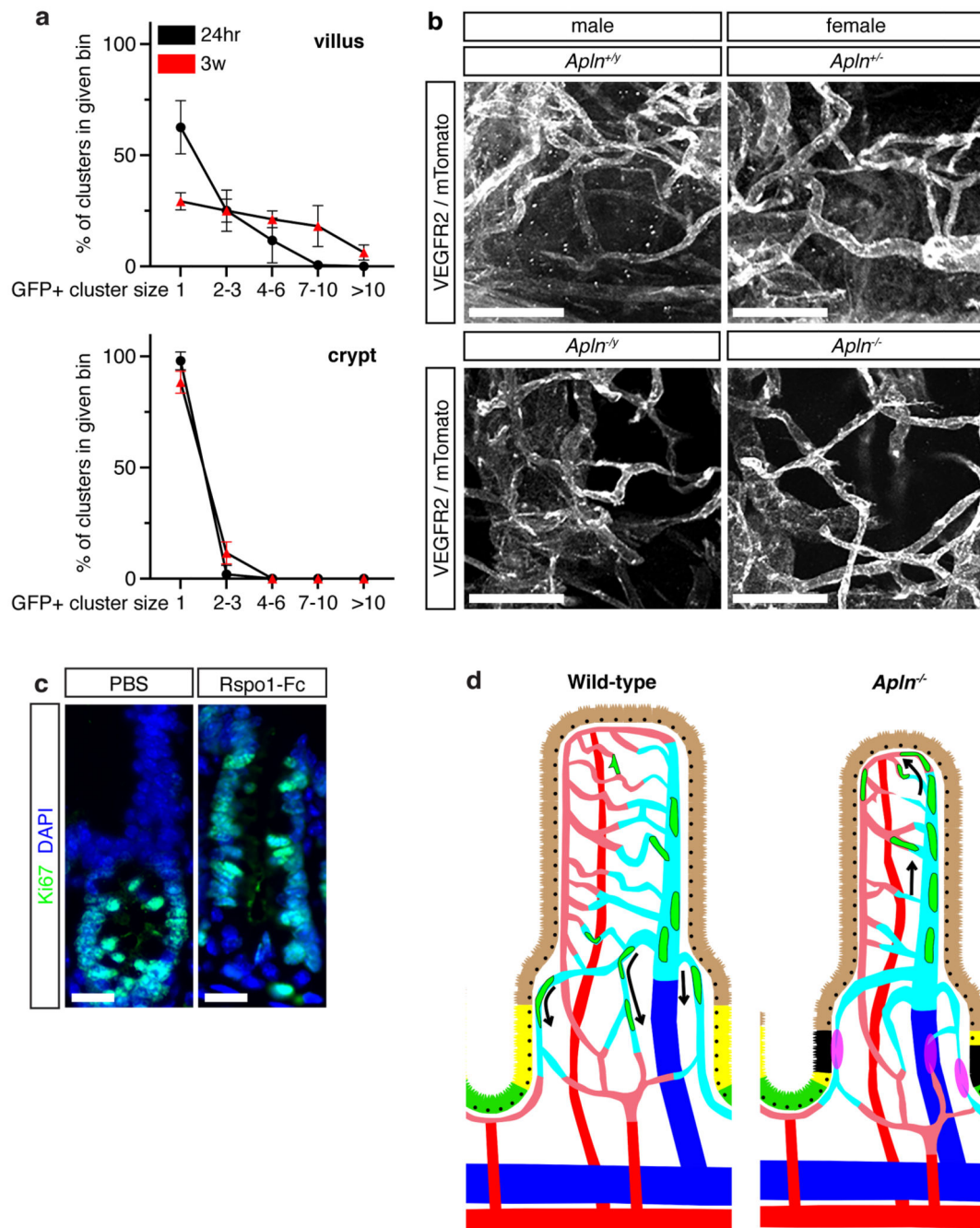
BECs ($p=0.0071$, $n=3$ sorted cell samples from individual mice) and **(d)** total intestine from control and *Apc*^{IEC} mice ($p=0.0051$, $n=4$ WT and $n=3$ *Apc*^{IEC} mice). **(e)** Paraffin section immunostaining for blood vessels (red, PECAM1) and in situ hybridization (ISH) for *Apln* (green). Zoomed areas marked by 1+2. **(f-h)** The majority of apelin-expressing endothelial cells are in or near the villus venule. **(f)** Whole-mount immunostaining of GFP expression (green) and either all intestinal vessels (white, VEGFR2/mTomato) or MADCAM1⁺ vessels (blue) in *Apln-CreERT2; mTmG* mice 24 hours post 4OHT injection. **(g)** Quantification of the percentage of GFP⁺ ECs that are in the MADCAM1⁺ villus venule or endothelial cells directly in contact with the villus venule (MADCAM1-adjacent) or crypt vessels in *Apln-CreERT2; mTmG* mice 24 hours post 4OHT injection ($n=3$ mice). **(h)** Quantification of percentage of GFP⁺ endothelial cells in the villus or crypt ($n=3$ mice). **(i)** *Aplnr* is widely expressed in the IVU. Paraffin section immunostaining/ISH for *Aplnr* (green) expressed on intestinal endothelial cells (red, PECAM1) of wild-type and *Apc*^{fl/fl}; *p53*^{fl/fl} *Vil-CreERT2* intestine; blue, DAPI. **(j)** *Apln* expression is maintained after VEGFR2 signaling blockade. Experimental setup for *AplnCreERT2; mTmG* lineage tracing combined with DC101 treatment. Whole-mount immunostaining for intestinal vessels (white, PECAM1) and GFP⁺ endothelial cells (green) after 24 hours of treatment with control or DC101 blocking antibodies. Red, ESM1; arrowheads, villus venule; arrows, capillary endothelial cells; asterisk, ESM1 staining comparison. Quantification of number of GFP⁺ endothelial cells in the villus or crypt, $n=4$ IgG treated and $n=5$ DC101 treated mice). Scale bars: 50 μm : e, f, j; 20 μm : b (insets), i. All data are shown as mean \pm SD. ** $P < 0.01$, *** $P < 0.001$ 2-tailed unpaired Student's *t* test. Images in e and i representative of 2 independent experiments.



Extended Data Fig. 6. Apelin maintains crypt venous capillary patency at steady state and during crypt expansion

(a-b) Neither vessel density nor blood endothelial cell (BEC) proliferation are decreased in *Apln*^{-/-} mice. (a) Quantification of crypt vessel density in control and *Apln*^{-/-} mice (p=0.0368, n=3 WT mice and n=4 *Apln*^{-/-} mice). (b) Quantification of percentage of villus and crypt Ki67⁺ BECs in control and *Apln*^{-/-} mice (n=8 WT mice and n=6 *Apln*^{-/-} mice). (c) Quantification of the number of empty collagen sleeves / villus area of wild-type and *Apln*^{-/-} mice (n=4 WT mice and n=3 *Apln*^{-/-} mice). (d) Venous identity of regressing crypt

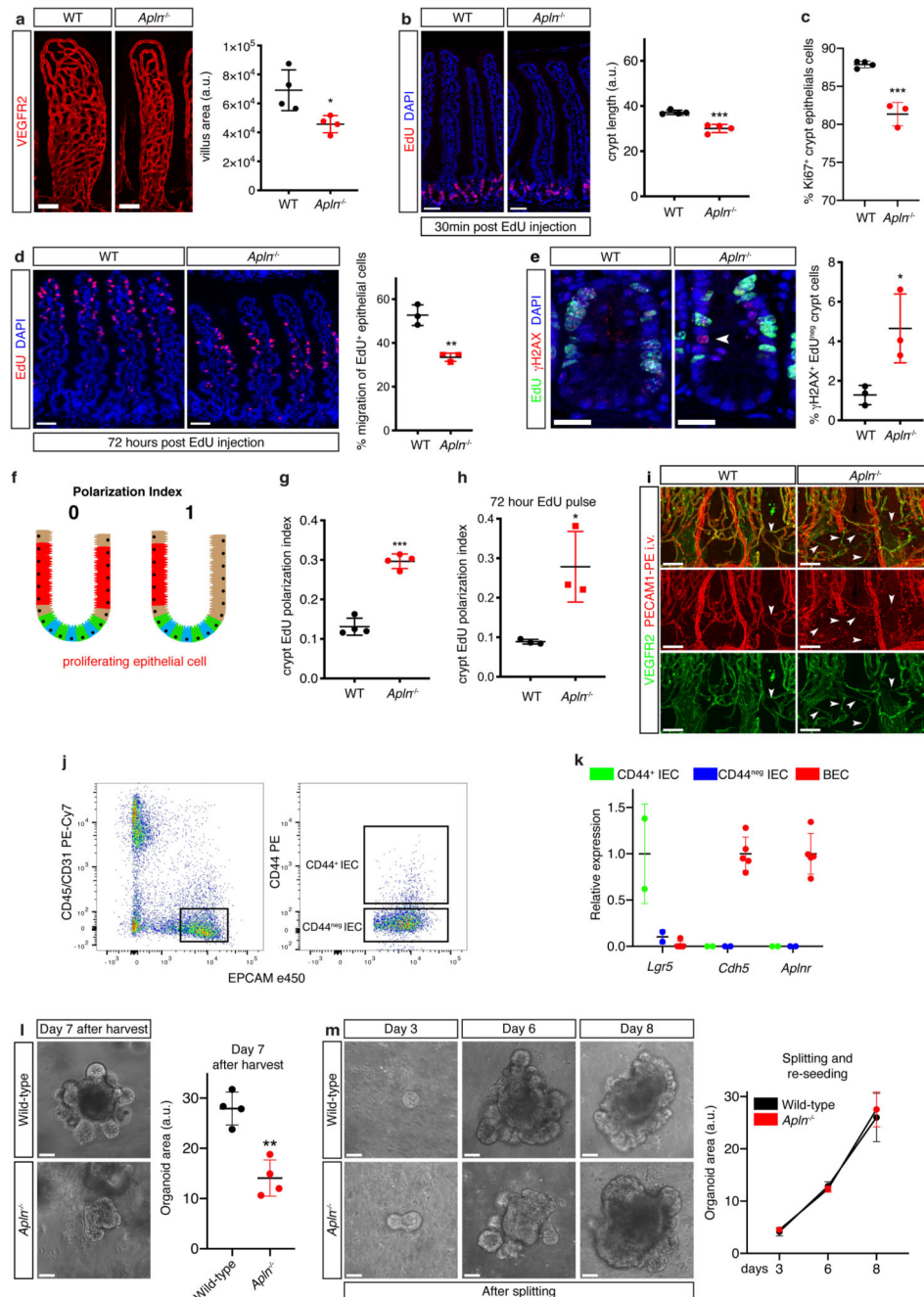
vessels in *Apln*^{-/-} mice. Whole-mount immunostaining for VEGFR2 (green), venous marker endomucin (red) and collagen IV (white). Arrowheads, empty collagen sleeves between endomucin⁺ vessels; arrow, regressing vessel. Quantification of number of regressed crypt vessels in *Apln*^{-/-} mice sorted by endomucin status of each end of regressed vessel (*n*=3 mice). (e) Quantification of crypt vessel density in *Apc*^{IEC} and *Apc*^{IEC}; *Apln*^{-/-} mice (*n*=3 *Apc*^{IEC} and *n*=4 *Apc*^{IEC}; *Apln*^{-/-} mice). (f) Quantification of percentage of villus and crypt Ki67⁺ BECs in *Apc*^{IEC} and *Apc*^{IEC}; *Apln*^{-/-} mice (*n*=4 mice). (g) Increased number of blind-ended crypt blood vessels in *Apc*^{IEC}; *Apln*^{-/-} mice. Whole-mount immunostaining of IVUs (red, VEGFR2) from *Apc*^{IEC} and *Apc*^{IEC}; *Apln*^{-/-} mice. Insets: blind-ended crypt vessels (arrowheads). (h) Increased empty collagen sleeves (green, collagen IV) in crypt vessels (red, VEGFR2) of *Apc*^{IEC}; *Apln*^{-/-} compared to *Apc*^{IEC} mice. Quantification of number of empty collagen sleeves per crypt vessel length (*p*=0.0002, *n*=5 *Apc*^{IEC} and *n*=4 *Apc*^{IEC}; *Apln*^{-/-} mice). (i) Venous identity of regressing crypt vessels in *Apc*^{IEC}; *Apln*^{-/-} mice. Whole-mount immunostaining of crypt vessels (green, VEGFR2) and venous identity marker endomucin (red) from *Apc*^{IEC} and *Apc*^{IEC}; *Apln*^{-/-} mice. Quantification of number of regressed crypt vessels in *Apc*^{IEC}; *Apln*^{-/-} mice sorted by endomucin status of each end of regressed vessel (*n*=4 mice). Scale bars: 50 μm: g-i; 20 μm: d, g+h (insets). All data are shown as mean ± SD. **P* < 0.05, ****P* < 0.001, 2-tailed unpaired Student's *t* test.



Extended Data Fig. 7. Clonal analysis of *Apln-CreERT2*; *mTmG* lineage tracing

(a) Clonal expansion of GFP⁺ cells in the villus, but not crypt vessels of *Apln-CreERT2*; *mTmG* mice. Analysis of venule and venule adjacent venous GFP⁺ cell cluster size in the villus and crypt after 24hr and 3 weeks of lineage tracing after 4-OHT injection, (mean ± SD, n=4 *Apln-CreERT2*; *mTmG* 24hr mice and n=3 *Apln-CreERT2*; *mTmG* 3w mice). (b) Lack of sex-specific differences in crypt vessel phenotype in *Apln*-deficient mice. Representative whole-mount immunostainings for crypt vessels (white, VEGFR2) in male and female mice heterozygous or null for *Apln*. (c) Paraffin section immunostaining for

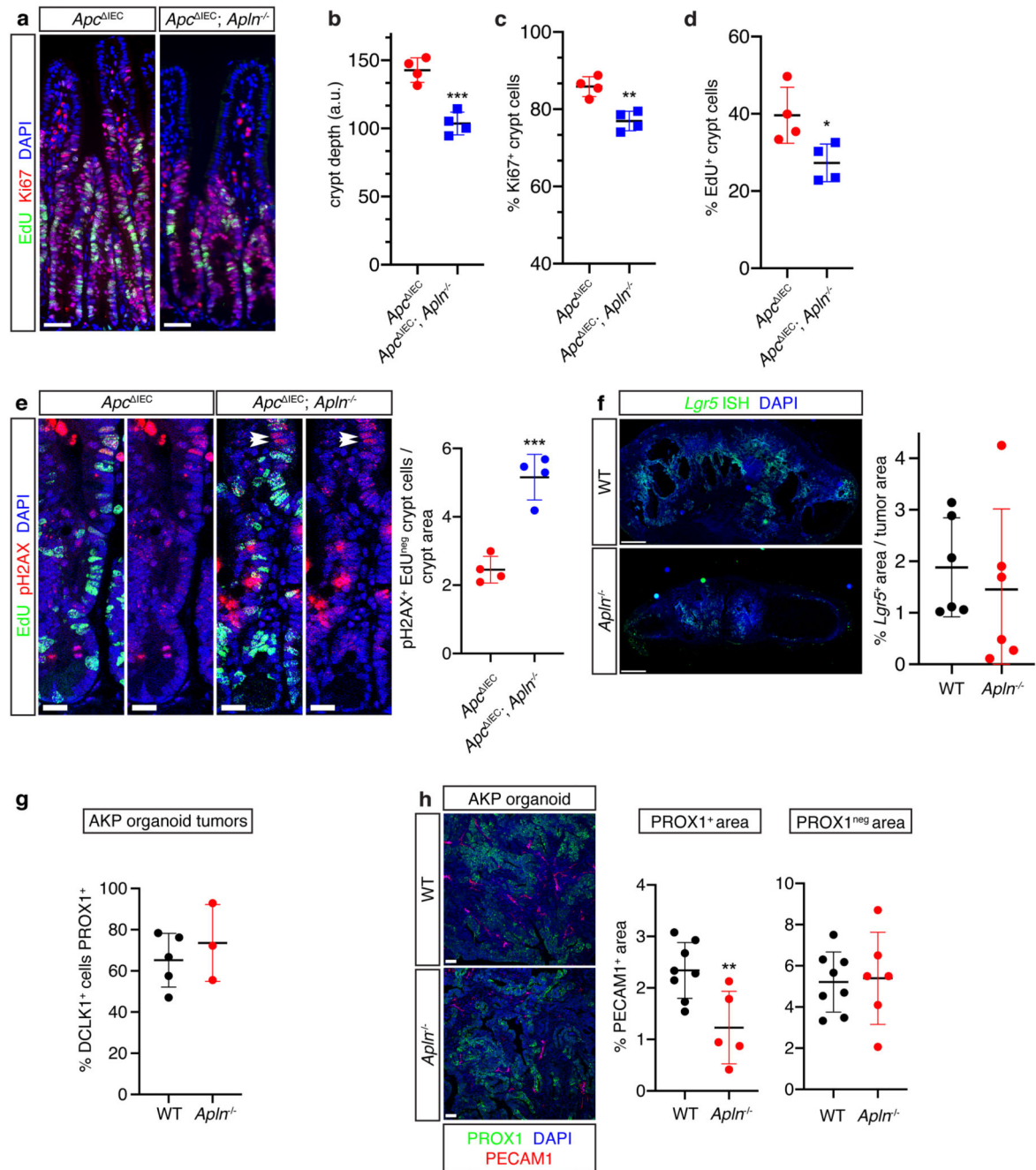
crypt proliferation (green, Ki67) in mice treated with PBS or Rspo1-FC for 4 days; blue, DAPI. **(d)** Model for APLN-mediated control of crypt vessel patency. APLN⁺ endothelial cells migrate during steady-state and expansion to the crypts in an APLN-dependent fashion. Scale bars: 50 μ m: b; 20 μ m: c. Images in a and c representative of 2 independent experiments.



Extended Data Fig. 8. Apelin promotes crypt perfusion and epithelial cell fitness

(a) Villi are smaller in *Apln*^{-/-} mice compared to controls. Whole-mount immunostaining for villus vessels (red, VEGFR2) in control and *Apln*^{-/-} mice. Quantification of villus area between control and *Apln*^{-/-} mice ($p=0.0221$, $n=4$ mice). (b) Crypt length is smaller in mice compared to controls. Paraffin section immunostaining; red, EdU; blue, DNA. Quantification of crypt length ($p=0.0004$, $n=4$ mice). (c) Decreased crypt epithelial cell proliferation in *Apln*^{-/-} mice. Quantification of the number of Ki67⁺ crypt epithelial cells in control and *Apln*^{-/-} mice ($p=0.0004$, $n=4$ WT mice and $n=3$ *Apln*^{-/-} mice). (d) Epithelial cell migration is slowed in *Apln*^{-/-} mice. Paraffin immunostaining for EdU (red) after 72h pulse; blue, DNA. Quantification of position of EdU⁺ epithelial cells 72h after pulse as a percentage of villus height ($p=0.0028$, $n=3$ mice). (e) Increased number of EdU^{neg} phospho- γ H2A.X⁺ crypt epithelial cells in *Apln*^{-/-} mice. Paraffin section immunostaining; green, EdU; red, phospho- γ H2A.X; blue, DNA. Quantification of percentage of crypt EdU^{neg} phospho- γ H2A.X⁺ epithelial cells ($p=0.032$, $n=3$ mice). (f) Definition of crypt epithelial proliferation polarization index. EdU⁺ crypt intestinal epithelial cells were annotated as either on the left or right side and the percentage of each to a side was used to generate a score where 0 indicates exactly the same number of EdU⁺ epithelial cells on each side of the crypt and 1 indicates all EdU⁺ epithelial cells are on one side of the crypt. (g) Crypt EdU⁺ epithelial cells are polarized on one side of the crypt in *Apln*^{-/-} mice. Polarization index of EdU⁺ crypt epithelial cells in control and *Apln*^{-/-} mice ($p<0.0001$, $n=4$ mice). (h) Pulsed EdU⁺ IECs are polarized on one side of the villus in *Apln*^{-/-} mice. Polarization index of EdU⁺ IECs after 72h pulse in control and *Apln*^{-/-} mice ($p=0.0214$, $n=3$ mice). (i) Decreased perfusion of crypt vessels in *Apln*^{-/-} mice. Whole-mount immunostaining for VEGFR2 (green) after i.v. injection of PE-conjugated PECAM1 antibody (red). Arrowheads: non-perfused VEGFR2⁺PECAM1-PE^{neg} vessels. (j) Density plots depicting the gating strategy for sorting CD44⁺ and CD44^{neg} epithelial cells using flow cytometry. Single, live CD45^{neg} CD31^{neg} cells expressing EPCAM were selected (left plot) and then collected as either CD44⁺ or CD44^{neg} epithelial cell subsets. (k) Apelin receptor is not expressed on intestinal epithelial cells (IECs). qPCR for *Lgr5*, *Cdh5* and *Aplnr* expression in CD44⁺ IECs (progenitor cells), CD44^{neg} IECs (differentiated IECs) and BECs ($n=2$ CD44⁺ sorted IECs, $n=2$ CD44^{neg} sorted IECs and $n=5$ sorted BECs from individual animals). (l, m) Defect of crypt epithelial progenitor survival in *Apln*^{-/-} mice is cell extrinsic. Images and quantification of organoid area from either wild-type or *Apln*^{-/-} mice after (l) first plating ($p=0.0013$) or (m) re-plating ($n=4$ organoid populations isolated from individual mice). Scale bars: 50 μ m: a, b, d, i, l, m; 20 μ m: e. All data are shown as mean \pm SD. * $P < 0.05$, ** $P < 0.01$, *** $P < 0.001$, 2-tailed unpaired Student's *t* test.

cells against top 100 genes of each cluster shown in (a). (c) Annotation of clusters used for GSEA analysis for genes up- and down-regulated in wild-type vs *Apln*^{-/-} crypt epithelial cells. (d) No increase in the number *Lgr5*-GFP stem cells (green, GFP, p=0.0266) or their proliferation (red, Ki67, p=0.0484) in *Apln*^{-/-} crypts; blue, DAPI (n=3 mice). (e, f) Decreased number of epithelial cells expressing tuft and enteroendocrine markers in *Apln*^{-/-} crypts. Paraffin section immunostaining for (e) DCLK1 (green) or (f) CHGA (red) in wild-type and *Apln*^{-/-} mice; blue, DAPI. Quantification of the number of (e) DCLK1⁺ (p=0.0188, WT vs *Apln*^{-/-} crypt) or (f) CHGA⁺ (p=0.0055, WT vs *Apln*^{-/-} crypt) in crypts and villi of wild-type and *Apln*^{-/-} mice (n=3 mice). Scale bars: 50 μm: e, f; 20 μm: d. *P < 0.05, **P < 0.01 2-tailed unpaired Student's t test.



Extended Data Fig. 10. Apelin maintains tumor progenitor cell fitness and proliferation.

(a-d) *Apln* deficiency reduces crypt expansion (a) Staining for EdU (green), Ki67 (red) and DNA (blue) in *Apc*^{IEC} and *Apc*^{IEC}; *Apln*^{-/-} mice. (b-d) Quantification for the (b) crypt depth (p=0.0007) and percentage of (c) Ki67⁺ (p=0.0026) and (d) EdU⁺ crypt IECs (p=0.0303, n=4 mice). (e) Increased number of EdU^{neg} phospho-γH2A.X⁺ crypt epithelial cells in *Apc*^{IEC}; *Apln*^{-/-} mice. Paraffin section immunostaining; green, EdU; red, phospho-γH2A.X; blue, DNA. Quantification of percentage of crypt EdU^{neg} phospho-γH2A.X⁺ epithelial cells (p=0.0004, n=4 mice). (f) In situ hybridization for *Lgr5* (green) in AKP

organoid tumors implanted into wild-type or *Apln*^{-/-} mice; DAPI, blue. Quantification for percentage of tumor area positive for *Lgr5* (n=6 tumors). (g) The majority of DCLK1⁺ cells in AKP organoid tumors also express PROX1. Quantification of percentage DCLK1⁺ cells that are also PROX1⁺ in either control or *Apln*^{-/-} mice (n=5 tumors in WT mice and n=3 tumors in *Apln*^{-/-} mice). (h) Apelin deficiency reduces vessel density in progenitor cell areas. Staining for progenitor marker PROX1 (green), PECAM1 (red) and DNA (blue) in AKP tumor grown in control and *Apln*^{-/-} mice. Quantification of tumor vascularization as percentage PECAM1⁺ area in PROX1⁺ (p=0.0082, n=8 tumors in WT mice and n=5 tumors in *Apln*^{-/-} mice) and PROX1^{neg} zones (n=8 tumors in WT mice and n=6 tumors in *Apln*^{-/-} mice) of AKP tumor organoids grown in control and *Apln*^{-/-} mice. Scale bars: 50 μm: a, f; 20 μm: e. All data are shown as mean ± SD. *P < 0.05, **P < 0.01, ***P < 0.001, 2-tailed unpaired Student's t test.

Supplementary Material

Refer to Web version on PubMed Central for supplementary material.

Acknowledgments

We thank Dr. Nathalie Piazzon (Institute of Pathology Biobank, CHUV and University of Lausanne, Lausanne, Switzerland) for providing human tumor samples, Dr. Matthias Lutolf for providing Rspo1-Fc, Ania Zuba, Marine Bruand and Marc LeCoutre for participation in the initial stages of this work, Céline Beauverd for mouse genotyping and colony maintenance and Dr. Sylvie Robine and Dr. Lena Claesson-Welsh for providing *Villin-CreERT2* and *Kdr^{fl/fl}; Cdh5-CreERT2* mice. The UNIL Animal, Cellular Imaging, Genomic Technologies, Mouse Pathology and Flow Cytometry Facilities and EPFL Histology Core and Protein Production facilities are gratefully acknowledged. We apologize to colleagues whose work we could not reference due to size constraints.

This work was supported by grants from the Swiss Cancer League (KLS 3406-02-2016 and KFS-4895-08-2019), Foundation MEDIC, the Emma Muschamp Foundation, the Swiss National Science Foundation (31003A-156266 to TVP, 31003A-166161 to SAL), the European Research Council (ERC EVOLVE-725051 to MDP) and the Gabriela Kummer MD-PhD fellowship and Alfred and Anneliese Sutter-Stöttner private fellowships (to CC).

Data availability

All data generated or analyzed are included in the main article and associated files. Gene expression profiling data were deposited in a Super Series (GSE178118) including both the intestinal blood endothelial (GSE111783) and epithelial cell data (GSE178110). Source data are provided with this paper.

References

1. Gehart H, Clevers H. Tales from the crypt: new insights into intestinal stem cells. *Nature Reviews Gastroenterology & Hepatology*. 2019; 16: 19–34. DOI: 10.1038/s41575-018-0081-y [PubMed: 30429586]
2. Zeuner A, Todaro M, Stassi G, De Maria R. Colorectal cancer stem cells: from the crypt to the clinic. *Cell Stem Cell*. 2014; 15: 692–705. DOI: 10.1016/j.stem.2014.11.012 [PubMed: 25479747]
3. Lu J, et al. Endothelial cells promote the colorectal cancer stem cell phenotype through a soluble form of Jagged-1. *Cancer Cell*. 2013; 23: 171–185. DOI: 10.1016/j.ccr.2012.12.021 [PubMed: 23375636]
4. De Palma M, Biziato D, Petrova TV. Microenvironmental regulation of tumour angiogenesis. *Nature Reviews Cancer*. 2017; 17: 457. doi: 10.1038/nrc.2017.51 [PubMed: 28706266]

5. Guinney J, et al. The consensus molecular subtypes of colorectal cancer. *Nat Med.* 2015; 21: 1350–1356. DOI: 10.1038/nm.3967 [PubMed: 26457759]
6. Lenz H-J, et al. Impact of consensus molecular subtype on survival in patients with metastatic colorectal cancer: results from CALGB/SWOG 80405 (Alliance). *J Clin Oncol.* 2019; 37: 1876–1885. DOI: 10.1200/jco.18.02258 [PubMed: 31042420]
7. Kerr RS, et al. Adjuvant capecitabine plus bevacizumab versus capecitabine alone in patients with colorectal cancer (QUASAR 2): an open-label, randomised phase 3 trial. *Lancet Oncol.* 2016; 17: 1543–1557. DOI: 10.1016/S1470-2045(16)30172-3 [PubMed: 27660192]
8. Kamba T, et al. VEGF-dependent plasticity of fenestrated capillaries in the normal adult microvasculature. *Am J Physiol Heart Circ Physiol.* 2006; 290: H560–H576. DOI: 10.1152/ajpheart.00133.2005 [PubMed: 16172168]
9. Bernier-Latmani J, Petrova TV. Intestinal lymphatic vasculature: structure, mechanisms and functions. *Nat Rev Gastroenterol Hepatol.* 2017; 14: 510–526. DOI: 10.1038/nrgastro.2017.79 [PubMed: 28655884]
10. de Sousa E Melo F, et al. Methylation of cancer-stem-cell-associated Wnt target genes predicts poor prognosis in colorectal cancer patients. *Cell Stem Cell.* 2011; 9: 476–485. DOI: 10.1016/j.stem.2011.10.008 [PubMed: 22056143]
11. Ragusa S, et al. PROX1 promotes metabolic adaptation and fuels outgrowth of Wnhigh metastatic colon cancer cells. *Cell Reports.* 2014; 8: 1957–1973. DOI: 10.1016/j.celrep.2014.08.041 [PubMed: 25242332]
12. Wiener Z, et al. Prox1 promotes expansion of the colorectal cancer stem cell population to fuel tumor growth and ischemia resistance. *Cell Reports.* 2014; 8: 1943–1956. DOI: 10.1016/j.celrep.2014.08.034 [PubMed: 25242330]
13. Petrova TV, et al. Transcription factor Prox1 induces colon cancer progression by promoting the transition from benign to highly dysplastic phenotype. *Cancer Cell.* 2008; 13: 407–419. DOI: 10.1016/j.ccr.2008.02.020 [PubMed: 18455124]
14. Rocha SF, et al. Esm1 modulates endothelial tip cell behavior and vascular permeability by enhancing VEGF bioavailability. *Circ Res.* 2014; doi: 10.1161/circresaha.115.304718
15. Yang Y, et al. Anti-VEGF- and anti-VEGF receptor-induced vascular alteration in mouse healthy tissues. *Proc Natl Acad Sci U S A.* 2013; 110: 12018–12023. DOI: 10.1073/pnas.1301331110 [PubMed: 23818623]
16. Korsisaari N, et al. Inhibition of VEGF-A prevents the angiogenic switch and results in increased survival of Apc+/min mice. *Proc Natl Acad Sci U S A.* 2007; 104: 10625–10630. DOI: 10.1073/pnas.0704213104 [PubMed: 17553957]
17. Carmeliet P, Jain RK. Molecular mechanisms and clinical applications of angiogenesis. *Nature.* 2011; 473: 298–307. [PubMed: 21593862]
18. Lundgren O. Studies on blood flow distribution and countercurrent exchange in the small intestine. *Acta Physiol Scand Suppl.* 1967; 303: 1–42. [PubMed: 5586813]
19. Witte L, et al. Monoclonal antibodies targeting the VEGF receptor-2 (Flk1/KDR) as an anti-angiogenic therapeutic strategy. *Cancer Metastasis Rev.* 1998; 17: 155–161. DOI: 10.1023/a:1006094117427 [PubMed: 9770111]
20. Sansom OJ, et al. Loss of Apc in vivo immediately perturbs Wnt signaling, differentiation, and migration. *Genes Dev.* 2004; 18: 1385–1390. DOI: 10.1101/gad.287404 [PubMed: 15198980]
21. Schepers AG, et al. Lineage tracing reveals Lgr5+ stem cell activity in mouse intestinal adenomas. *Science.* 2012; 337: 730–735. DOI: 10.1126/science.1224676 [PubMed: 22855427]
22. Corbett TH, Griswold DP, Roberts BJ, Peckham JC, Schabel FM. Tumor induction relationships in development of transplantable cancers of the colon in mice for chemotherapy assays, with a note on carcinogen structure. *Cancer Res.* 1975; 35: 2434–2439. [PubMed: 1149045]
23. Jinushi M, et al. Milk fat globule epidermal growth factor–8 blockade triggers tumor destruction through coordinated cell-autonomous and immune-mediated mechanisms. *J Exp Med.* 2009; 206: 1317–1326. DOI: 10.1084/jem.20082614 [PubMed: 19433619]
24. Dalerba P, et al. Phenotypic characterization of human colorectal cancer stem cells. *Proc Natl Acad Sci U S A.* 2007; 104: 10158–10163. DOI: 10.1073/pnas.0703478104 [PubMed: 17548814]

25. Ragusa S, et al. Antiangiogenic immunotherapy suppresses desmoplastic and chemoresistant intestinal tumors in mice. *J Clin Invest.* 2020; 130: 1199–1216. DOI: 10.1172/JCI129558 [PubMed: 32015230]
26. McKenzie JAG, et al. Apelin is required for non-neovascular remodeling in the retina. *Am J Pathol.* 2012; 180: 399–409. DOI: 10.1016/j.ajpath.2011.09.035 [PubMed: 22067912]
27. Langen UH, et al. Cell–matrix signals specify bone endothelial cells during developmental osteogenesis. *Nat Cell Biol.* 2017; 19: 189–201. DOI: 10.1038/ncb3476 [PubMed: 28218908]
28. Chen Q, et al. Apelin+ endothelial niche cells control hematopoiesis and mediate vascular regeneration after myeloablative injury. *Cell Stem Cell.* 2019; doi: 10.1016/j.stem.2019.10.006
29. Kidoya H, et al. The apelin/APJ system induces maturation of the tumor vasculature and improves the efficiency of immune therapy. *Oncogene.* 2012; 31: 3254 doi: 10.1038/onc.2011.489 [PubMed: 22037214]
30. Kidoya H, et al. APJ regulates parallel alignment of arteries and veins in the skin. *Dev Cell.* 2015; 33: 247–259. DOI: 10.1016/j.devcel.2015.02.024 [PubMed: 25920569]
31. Kidoya H, Takakura N. Biology of the apelin-APJ axis in vascular formation. *The Journal of Biochemistry.* 2012; 152: 125–131. DOI: 10.1093/jb/mvs071 [PubMed: 22745157]
32. Tian X, et al. Subepicardial endothelial cells invade the embryonic ventricle wall to form coronary arteries. *Cell Res.* 2013; 23: 1075–1090. DOI: 10.1038/cr.2013.83 [PubMed: 23797856]
33. Lee H-O, et al. Lineage-dependent gene expression programs influence the immune landscape of colorectal cancer. *Nat Genet.* 2020; 52: 594–603. DOI: 10.1038/s41588-020-0636-z [PubMed: 32451460]
34. Kuba K, et al. Impaired heart contractility in apelin gene–deficient mice associated with aging and pressure overload. *Circ Res.* 2007; 101: e32–e42. DOI: 10.1161/CIRCRESAHA.107.158659 [PubMed: 17673668]
35. Baluk P, Morikawa S, Haskell A, Mancuso M, McDonald DM. Abnormalities of basement membrane on blood vessels and endothelial sprouts in tumors. *Am J Pathol.* 2003; 163: 1801–1815. DOI: 10.1016/S0002-9440(10)63540-7 [PubMed: 14578181]
36. Kim KA, et al. Mitogenic influence of human R-spondin1 on the intestinal epithelium. *Science.* 2005; 309: 1256–1259. DOI: 10.1126/science.1112521 [PubMed: 16109882]
37. Ootani A, et al. Sustained in vitro intestinal epithelial culture within a Wnt-dependent stem cell niche. *Nat Med.* 2009; 15: 701–706. DOI: 10.1038/nm.1951 [PubMed: 19398967]
38. Hua G, et al. Crypt base columnar stem cells in small intestines of mice are radioresistant. *Gastroenterology.* 2012; 143: 1266–1276. DOI: 10.1053/j.gastro.2012.07.106 [PubMed: 22841781]
39. Yan KS, et al. Intestinal enteroendocrine lineage cells possess homeostatic and injury-inducible stem cell activity. *Cell Stem Cell.* 2017; 21: 78–90. e76 doi: 10.1016/j.stem.2017.06.014 [PubMed: 28686870]
40. Nakanishi Y, et al. Dclk1 distinguishes between tumor and normal stem cells in the intestine. *Nat Genet.* 2013; 45: 98–103. DOI: 10.1038/ng.2481 [PubMed: 23202126]
41. Westphalen CB, et al. Long-lived intestinal tuft cells serve as colon cancer-initiating cells. *J Clin Invest.* 2014; 124: 1283–1295. DOI: 10.1172/JCI73434 [PubMed: 24487592]
42. Frentzas S, et al. Vessel co-option mediates resistance to anti-angiogenic therapy in liver metastases. *Nat Med.* 2016; 22: 1294 doi: 10.1038/nm.4197 [PubMed: 27748747]
43. Mohyeldin A, Garzón-Muvdi T, Quiñones-Hinojosa A. Oxygen in stem cell biology: a critical component of the stem cell niche. *Cell Stem Cell.* 2010; 7: 150–161. DOI: 10.1016/j.stem.2010.07.007 [PubMed: 20682444]
44. Sancho P, Barneda D, Heeschen C. Hallmarks of cancer stem cell metabolism. *Br J Cancer.* 2016; 114: 1305 doi: 10.1038/bjc.2016.152 [PubMed: 27219018]
45. La Vecchia S, Sebastián C. Metabolic pathways regulating colorectal cancer initiation and progression. *Semin Cell Dev Biol.* 2020; 98: 63–70. DOI: 10.1016/j.semcdb.2019.05.018 [PubMed: 31129171]
46. Pitulescu ME, et al. Dll4 and Notch signalling couples sprouting angiogenesis and artery formation. *Nat Cell Biol.* 2017; 19: 915–927. DOI: 10.1038/ncb3555 [PubMed: 28714968]

47. Xu C, et al. Arteries are formed by vein-derived endothelial tip cells. *Nat Commun.* 2014; 5 5758 doi: 10.1038/ncomms6758 [PubMed: 25502622]
48. Lee HW, et al. The Role of Venous Endothelial Cells in Developmental and Pathologic Angiogenesis. *Circulation.* 2021; doi: 10.1161/circulationaha.121.054071
49. Kasai A, et al. Retardation of retinal vascular development in apelin-deficient mice. *Arterioscl Throm Vas.* 2008; 28: 1717–1722. DOI: 10.1161/atvbaha.108.163402
50. Kasai A, et al. Apelin is a crucial factor for hypoxia-induced retinal angiogenesis. *Arterioscl Throm Vas.* 2010; 30: 2182–2187. DOI: 10.1161/atvbaha.110.209775
51. Eyries M, et al. Hypoxia-induced apelin expression regulates endothelial cell proliferation and regenerative angiogenesis. *Circ Res.* 2008; 103: 432–440. DOI: 10.1161/CIRCRESAHA.108.179333 [PubMed: 18617693]
52. Liu Q, et al. Genetic targeting of sprouting angiogenesis using Aplin-CreER. *Nat Commun.* 2015; 6: 6020. doi: 10.1038/ncomms7020 [PubMed: 25597280]
53. Mastrella G, et al. Targeting APLN/APLNR improves antiangiogenic efficiency and blunts proinvasive side effects of VEGFA/VEGFR2 blockade in glioblastoma. *Cancer Res.* 2019; 79: 2298–2313. DOI: 10.1158/0008-5472.Can-18-0881 [PubMed: 30718358]
54. Uribealago I, et al. Apelin inhibition prevents resistance and metastasis associated with anti-angiogenic therapy. *EMBO Mol Med.* 2019; 11 e9266 doi: 10.15252/emmm.201809266 [PubMed: 31267692]
55. Zuurbier L, et al. Apelin: A putative novel predictive biomarker for bevacizumab response in colorectal cancer. *Oncotarget.* 2017; 8: 42949–42961. DOI: 10.18632/oncotarget.17306 [PubMed: 28487489]
56. Jaiprasart P, Dogra S, Neelakantan D, Devapatla B, Woo S. Identification of signature genes associated with therapeutic resistance to anti-VEGF therapy. *Oncotarget.* 2020; 11: 99–114. DOI: 10.18632/oncotarget.27307 [PubMed: 32002127]
57. Zhang L, Takara K, Yamakawa D, Kidoya H, Takakura N. Apelin as a marker for monitoring the tumor vessel normalization window during antiangiogenic therapy. *Cancer Sci.* 2016; 107: 36–44. DOI: 10.1111/cas.12836 [PubMed: 26475217]
58. Lathen C, et al. ERG-APLNR axis controls pulmonary venule endothelial proliferation in pulmonary veno-occlusive disease. *Circulation.* 2014; 130: 1179–1191. DOI: 10.1161/CIRCULATIONAHA.113.007822 [PubMed: 25062690]
59. Strohbach A, et al. The apelin receptor influences biomechanical and morphological properties of endothelial cells. *J Cell Physiol.* 2018; 233: 6250–6261. DOI: 10.1002/jcp.26496 [PubMed: 29369349]
60. Sharma B, et al. Alternative Progenitor Cells Compensate to Rebuild the Coronary Vasculature in Elabela- and Apj-Deficient Hearts. *Dev Cell.* 2017; 42: 655–666. e653 doi: 10.1016/j.devcel.2017.08.008 [PubMed: 28890073]
61. Shibata H, et al. Rapid colorectal adenoma formation initiated by conditional targeting of the Apc gene. *Science.* 1997; 278: 120–123. DOI: 10.1126/science.278.5335.120 [PubMed: 9311916]
62. Barker N, et al. Identification of stem cells in small intestine and colon by marker gene Lgr5. *Nature.* 2007; 449: 1003–1007. [PubMed: 17934449]
63. Marino S, Vooijs M, van der Gulden H, Jonkers J, Berns A. Induction of medulloblastomas in p53-null mutant mice by somatic inactivation of Rb in the external granular layer cells of the cerebellum. *Genes Dev.* 2000; 14: 994–1004. [PubMed: 10783170]
64. Jackson EL, et al. Analysis of lung tumor initiation and progression using conditional expression of oncogenic K-ras. *Genes Dev.* 2001; 15: 3243–3248. DOI: 10.1101/gad.943001 [PubMed: 11751630]
65. El Marjou F, et al. Tissue-specific and inducible Cre-mediated recombination in the gut epithelium. *Genesis.* 2004; 39: 186–193. DOI: 10.1002/gene.20042 [PubMed: 15282745]
66. Moser AR, Pitot HC, Dove WF. A dominant mutation that predisposes to multiple intestinal neoplasia in the mouse. *Science.* 1990; 247: 322–324. DOI: 10.1126/science.2296722 [PubMed: 2296722]
67. Muzumdar MD, Tasic B, Miyamichi K, Li L, Luo L. A global double-fluorescent Cre reporter mouse. *Genesis.* 2007; 45: 593–605. DOI: 10.1002/dvg.20335 [PubMed: 17868096]

68. Hooper AT, et al. Engraftment and reconstitution of hematopoiesis is dependent on Vegfr2-mediated regeneration of sinusoidal endothelial cells. *Cell Stem Cell*. 2009; 4: 263–274. DOI: 10.1016/j.stem.2009.01.006 [PubMed: 19265665]
69. Sörensen I, Adams RH, Gossler A. DLL1-mediated Notch activation regulates endothelial identity in mouse fetal arteries. *Blood*. 2009; 113: 5680–5688. DOI: 10.1182/blood-2008-08-174508 [PubMed: 19144989]
70. Harvey NL, et al. Lymphatic vascular defects promoted by Prox1 haploinsufficiency cause adult-onset obesity. *Nat Genet*. 2005; 37: 1072–1081. DOI: 10.1038/ng1642 [PubMed: 16170315]
71. Bernier-Latmani J, Petrova TV. High-resolution 3D analysis of mouse small-intestinal stroma. *Nat Protoc*. 2016; 11: 1617–1629. DOI: 10.1038/nprot.2016.092 [PubMed: 27560169]
72. Yang B, et al. Single-cell phenotyping within transparent intact tissue through whole-body clearing. *Cell*. 2014; 158: 945–958. DOI: 10.1016/j.cell.2014.07.017 [PubMed: 25088144]
73. Sato T, et al. Single Lgr5 stem cells build crypt / villus structures in vitro without a mesenchymal niche. *Nature*. 2009; 459: 262–265. DOI: 10.1038/nature07935 [PubMed: 19329995]
74. Squadrito, Mario L ; , et al. miR-511-3p modulates genetic programs of tumor-associated macrophages. *Cell Reports*. 2012; 1: 141–154. DOI: 10.1016/j.celrep.2011.12.005 [PubMed: 22832163]
75. Carvalho BS, Irizarry RA. A framework for oligonucleotide microarray preprocessing. *Bioinformatics*. 2010; 26: 2363–2367. DOI: 10.1093/bioinformatics/btq431 [PubMed: 20688976]
76. Ritchie ME, et al. limma powers differential expression analyses for RNA-sequencing and microarray studies. *Nucleic Acids Res*. 2015; 43: e47. doi: 10.1093/nar/gkv007 [PubMed: 25605792]
77. Dobin A, et al. STAR: ultrafast universal RNA-seq aligner. *Bioinformatics*. 2013; 29: 15–21. DOI: 10.1093/bioinformatics/bts635 [PubMed: 23104886]
78. Anders S, Pyl PT, Huber W. HTSeq—a Python framework to work with high-throughput sequencing data. *Bioinformatics*. 2015; 31: 166–169. DOI: 10.1093/bioinformatics/btu638 [PubMed: 25260700]
79. Love MI, Huber W, Anders S. Moderated estimation of fold change and dispersion for RNA-seq data with DESeq2. *Genome Biol*. 2014; 15: 550. doi: 10.1186/s13059-014-0550-8 [PubMed: 25516281]
80. Subramanian A, et al. Gene set enrichment analysis: A knowledge-based approach for interpreting genome-wide expression profiles. *Proc Natl Acad Sci U S A*. 2005; 102: 15545–15550. DOI: 10.1073/pnas.0506580102 [PubMed: 16199517]
81. Liberzon A, et al. The Molecular Signatures Database (MSigDB) hallmark gene set collection. *Cell Syst*. 2015; 1: 417–425. DOI: 10.1016/j.cels.2015.12.004 [PubMed: 26771021]
82. Masiero M, et al. A core human primary tumor angiogenesis signature identifies the endothelial orphan receptor ELTD1 as a key regulator of angiogenesis. *Cancer Cell*. 2013; 24: 229–241. DOI: 10.1016/j.ccr.2013.06.004 [PubMed: 23871637]
83. Stuart T, et al. Comprehensive integration of single-cell data. *Cell*. 2019; 177: 1888–1902. e1821 doi: 10.1016/j.cell.2019.05.031 [PubMed: 31178118]
84. Zudaire E, Gambardella L, Kurcz C, Vermeren S. A computational tool for quantitative analysis of vascular networks. *PLoS ONE*. 2011; 6 e27385 doi: 10.1371/journal.pone.0027385 [PubMed: 22110636]
85. Skog M, et al. Expression and prognostic value of transcription factor PROX1 in colorectal cancer. *Br J Cancer*. 2011; 105: 1346–1351. DOI: 10.1038/bjc.2011.297 [PubMed: 21970873]

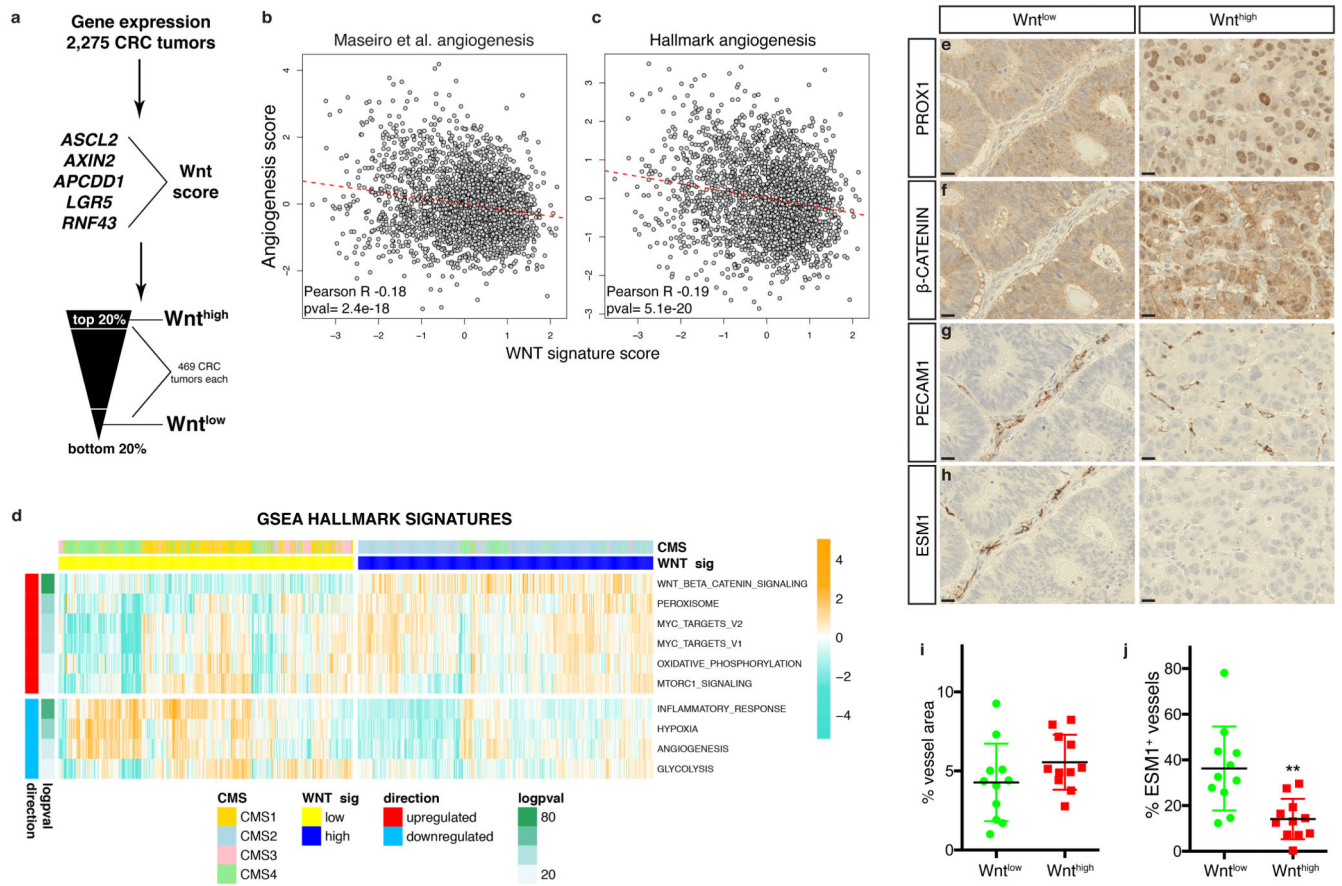


Fig. 1. Low VEGFA signaling and normoxia are hallmarks of Wnt^{high} CRC.

(a) Scheme for Wnt score generation from 2,275 CRC tumor gene expression profiles (see Supplementary Table 1). (b, c) Correlation analysis between WNT signature score and (b) VEGFA-dependent angiogenesis signature⁸² or (c) Hallmark angiogenesis signature, dashed line indicates linear regression fit, n=469 tumors. (d) Wnt^{high} CRC tumors are characterized by O₂-demanding metabolic pathways, low hypoxia, angiogenesis and glycolysis. Subset of GSEA Hallmark signatures up- or downregulated in Wnt^{high} CRC tumors (full set, Supplementary Fig. 1). (e-g) Immunostaining of human Wnt^{neg} or Wnt^{high} CRC tumors for (e) PROX1, (f) β-CATENIN, (g) PECAM1 and (h) ESM1. Indicated markers are stained in brown while cell nuclei are counterstained with haematoxylin in blue. (i-j) Quantification of percentage of (i) total vessel area or (j) ESM1⁺ vessels in Wnt^{low} or Wnt^{high} CRC tumors (p=0.0018, n=11 tumors). Scale bars: 20 μm. All data are shown as mean ± SD. **P < 0.01, 2-tailed unpaired Student's *t* test.

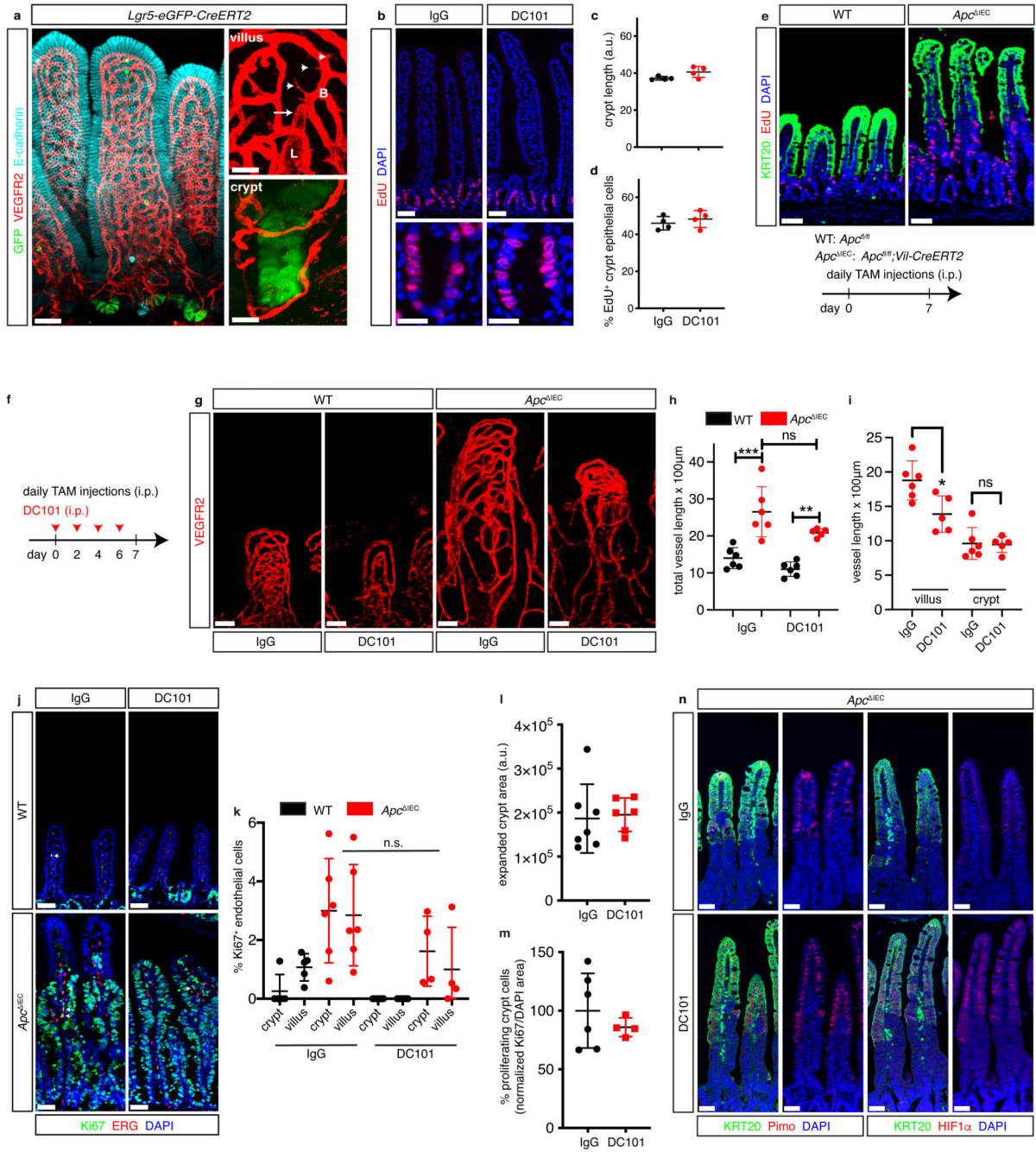


Fig. 2. Normal and transformed stem/progenitor cells are maintained in a normoxic VEGFA-independent niche.

(a) Whole-mount immunostaining of intestinal blood vessels (red, VEGFR2) and epithelial cells (cyan, E-cadherin) in *Lgr5-EGFP-CreERT2* mice. Intestinal stem cells express GFP (green). High magnification images show presence of endothelial (B) filopodia in villus (arrowheads), but not crypt blood vessels. The villus lymphatic capillary (L and arrow) is also VEGFR2⁺. (b-d) The crypt length and number of EdU⁺ crypt epithelial cells (red) are unchanged after DC101 treatment. Quantification of (c) crypt length and (d) number

of EdU⁺ crypt cells, $n=4$ mice. **(e)** Acute epithelial *Apc* loss-of-function rapidly expands intestinal crypts. Control and *Apc*^{IEC} mice were injected with tamoxifen and analyzed after 7 days. Expanded crypt epithelial cells (red, EdU) do not express differentiation marker KRT20 (green). Representative of at least 3 independent experiments. **(f)** Experimental design of epithelial *Apc* loss-of-function combined with VEGFR2 blockade. **(g)** Crypt vessel (red, VEGFR2) length is not changed after DC101 treatment. **(h-i)** Quantification of **(h)** total vessel length (x100 μm), ($p=0.0002$, WT IgG vs *Apc*^{IEC} IgG; $p=0.0034$, WT DC101 vs *Apc*^{IEC} DC101) and **(i)** villus and crypt vessel length (x100 μm), ($p=0.0186$, villus IgG vs villus DC101) in *Apc*^{IEC} intestine treated with control IgG or DC101, $n=6$ mice. **(j, k)** Intestinal endothelial cell proliferation is maintained during VEGFR2 blockade in *Apc*^{IEC} mice. **(j)** Ki67⁺ (green) endothelial cell nuclei (red, ERG) are present in both villus and crypt area in *Apc*^{IEC} mice during VEGFR2 blockade; blue, DAPI. **(k)** Quantification of percentage of Ki67⁺ blood endothelial cells in either crypt or villus vessels in control or *Apc*^{IEC} mice treated with control or DC101 antibodies ($n=5$ WT IgG-treated mice; $n=6$ WT DC101-treated mice, $n=6$ *Apc*^{IEC} IgG-treated mice and $n=4$ *Apc*^{IEC} DC101-treated mice). **(l, m)** Crypt expansion is insensitive to VEGFR2 blockade. Quantification of **(l)** expanded crypt size ($n=7$ IgG and $n=6$ DC101-treated *Apc*^{IEC} mice) and **(m)** percentage Ki67⁺ epithelial cells in control IgG- or DC101-treated *Apc*^{IEC} mice ($n=6$ IgG and $n=4$ DC101-treated *Apc*^{IEC} mice). **(n)** The expanded progenitor niche is normoxic. Hypoxia (red, pimonidazole (Pimo), or HIF1 α) is limited to differentiated epithelial cells (green, KRT20) in *Apc*^{IEC} mice. Note absence of hypoxic marker staining in crypts. Representative of at least 3 independent experiments. Scale bars: 50 μm ; 20 μm : a and b (insets). All data are shown as mean \pm SD. * $P < 0.05$, ** $P < 0.01$, *** $P < 0.001$, 2-tailed unpaired Student's *t* test or one-way ANOVA with Bonferroni's (h, i) or Tukey's (k) correction for multiple comparisons.

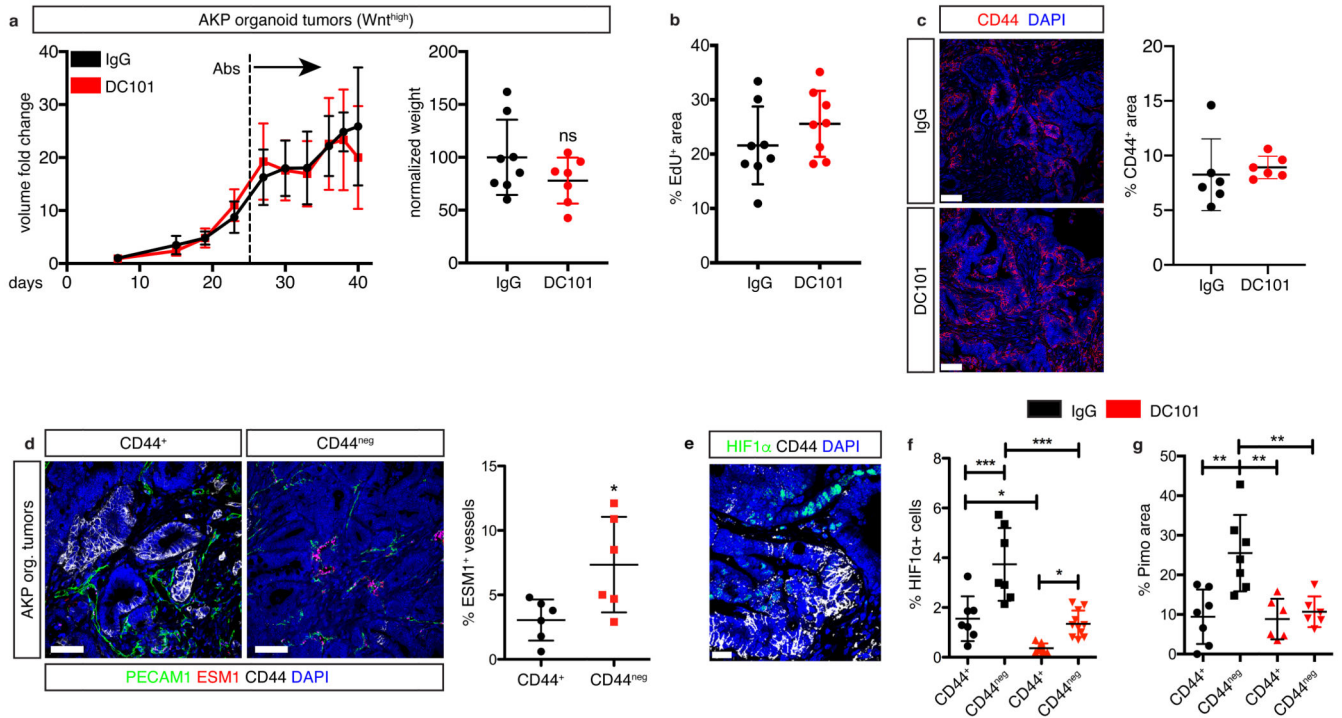


Fig. 3. Wnt^{high} CRC stem/progenitor cells are maintained in a normoxic VEGFA-independent niche.

(a-c) VEGFR2 blockade does not hinder AKP organoid tumor growth, proliferation or stem/progenitor cell maintenance. Quantification of subcutaneous AKP tumor organoid (a) volume and weight ($n=8$ IgG-treated tumors and $n=7$ DC101-treated tumors) and (b) percentage EdU⁺ epithelial cells in control antibody- and DC101-treated mice, ($n=8$ IgG-treated tumors and $n=7$ DC101-treated tumors). Data from two independent experiments. (c) VEGFR2 blockade does not decrease AKP organoid tumor progenitor cell numbers. Paraffin section immunostaining and quantification of percentage CD44⁺ progenitors (red) in control antibody- and DC101-treated mice AKP tumors ($n=6$ tumors). (d) Decreased VEGFA signaling in progenitor cell zones of AKP organoid tumors. Paraffin section immunostaining of ESM1⁺ (red) blood vessels (green, PECAM1) in CD44⁺ (white) and CD44^{neg} areas of AKP organoid tumors; blue, DNA. Quantification of percentage ESM1⁺ blood vessels in CD44⁺ and CD44^{neg} tumor areas, $n=6$. (e-g) The AKP tumor organoid progenitor cell niche is less hypoxic than zones with more differentiated tumor cells. (e) Paraffin section immunostaining of AKP tumor progenitor cells (white, CD44) and HIF1 α ⁺ cells (green) and DNA (blue). Quantification of percentage (f) HIF1 α ⁺ CD44⁺ or CD44^{neg} cells ($n=7$ IgG-treated and $n=10$ DC101-treated tumors; $p=0.0001$ CD44⁺ IgG vs CD44^{neg} IgG, $p=0.0282$ CD44⁺ IgG vs CD44⁺ DC101, $p<0.0001$ CD44^{neg} IgG vs CD44^{neg} DC101, $p=0.0456$ CD44⁺ DC101 vs CD44^{neg} DC101) or (g) Hypoxic pimonidazole⁺ CD44⁺ or CD44^{neg} cells in AKP tumors of control antibody- and DC101-treated mice ($n=7$ IgG-treated and $n=6$ DC101-treated tumors; $p=0.0015$ CD44⁺ IgG vs CD44^{neg} IgG, $p=0.0016$ CD44^{neg} IgG vs CD44⁺ DC101, $p=0.0051$ CD44^{neg} IgG vs CD44^{neg} DC101). Scale bars: 50 μ m: c, d; 20 μ m: E. All data are shown as mean \pm SD. * $P < 0.05$, ** $P < 0.01$, *** $P < 0.001$, 2-tailed unpaired Student's t test and one-way ANOVA with Bonferroni's correction (f, g).

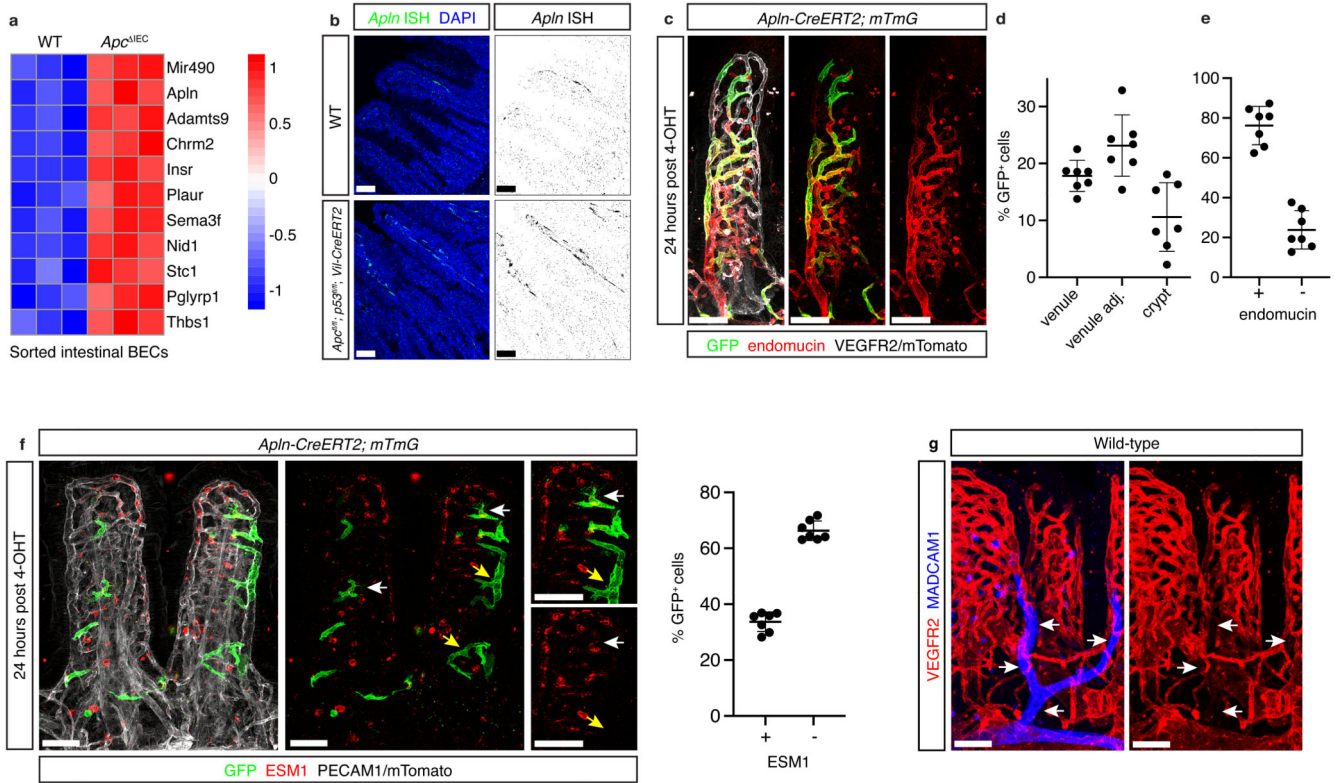


Fig. 4. Acute progenitor expansion induces endothelial apelin expression.

(a) Transcripts upregulated at least two-fold in *Apc^{IEC}* sorted intestinal blood endothelial cells (BECs) compared to WT controls, $n=3$ mice. (b) *Apln* ISH (green, right; black, left) in normal and Wnt-driven expanded crypts from control and *Apc^{fl/fl}; p53^{fl/fl}; Vil-CreERT2* intestine; blue, DNA. (c) Apelin expression is restricted to intestinal endothelial cells. Whole-mount immunostaining of GFP expression (green) and intestinal vessels (white, VEGFR2/mTomato) in *Apln-CreERT2; mTmG* mice 24 hours post 4-OHT injection. The majority of GFP⁺ cells co-express venous marker endomucin (red). (d) Almost half of apelin-expressing endothelial cells are observed in the villus venule or in vessels adjacent to the main venule, while on average 10% of GFP⁺ endothelial cells were found in crypt vessels. Quantification of the percentage of GFP⁺ endothelial cells that are in the villus venule, directly in contact with the villus venule (venule adj.) or crypt vessels in *Apln-CreERT2; mTmG* mice 24 hours post 4OHT injection ($n=6$ mice). (e) The majority of apelin-expressing endothelial cells are endomucin⁺. Quantification of the percentage of GFP⁺ endomucin⁺ endothelial cells ($n=6$ mice). (f) The majority of apelin-expressing endothelial cells are ESM1^{neg}. Whole-mount immunostaining of GFP expression (green) co-stained for ESM1 (red) in intestinal vessels (white, VEGFR2/mTomato) in *Apln-CreERT2; mTmG* mice 24 hours post 4-OHT injection. Arrowheads indicate ESM1⁺ (white) and ESM1^{neg} (yellow) GFP⁺ cells. Quantification of the percentage of ESM1^{neg} GFP⁺ endothelial cells ($n=6$ mice). (g) Low VEGFR2 expression in villus venules. Whole-mount immunostaining for intestinal venules (blue, MADCAM1) and all intestinal vessels (red, VEGFR2). Arrowheads highlight VEGFR2-low venules. Representative of at least 3 independent experiments. Scale bars: 50 μ m. All data are shown as mean \pm SD.

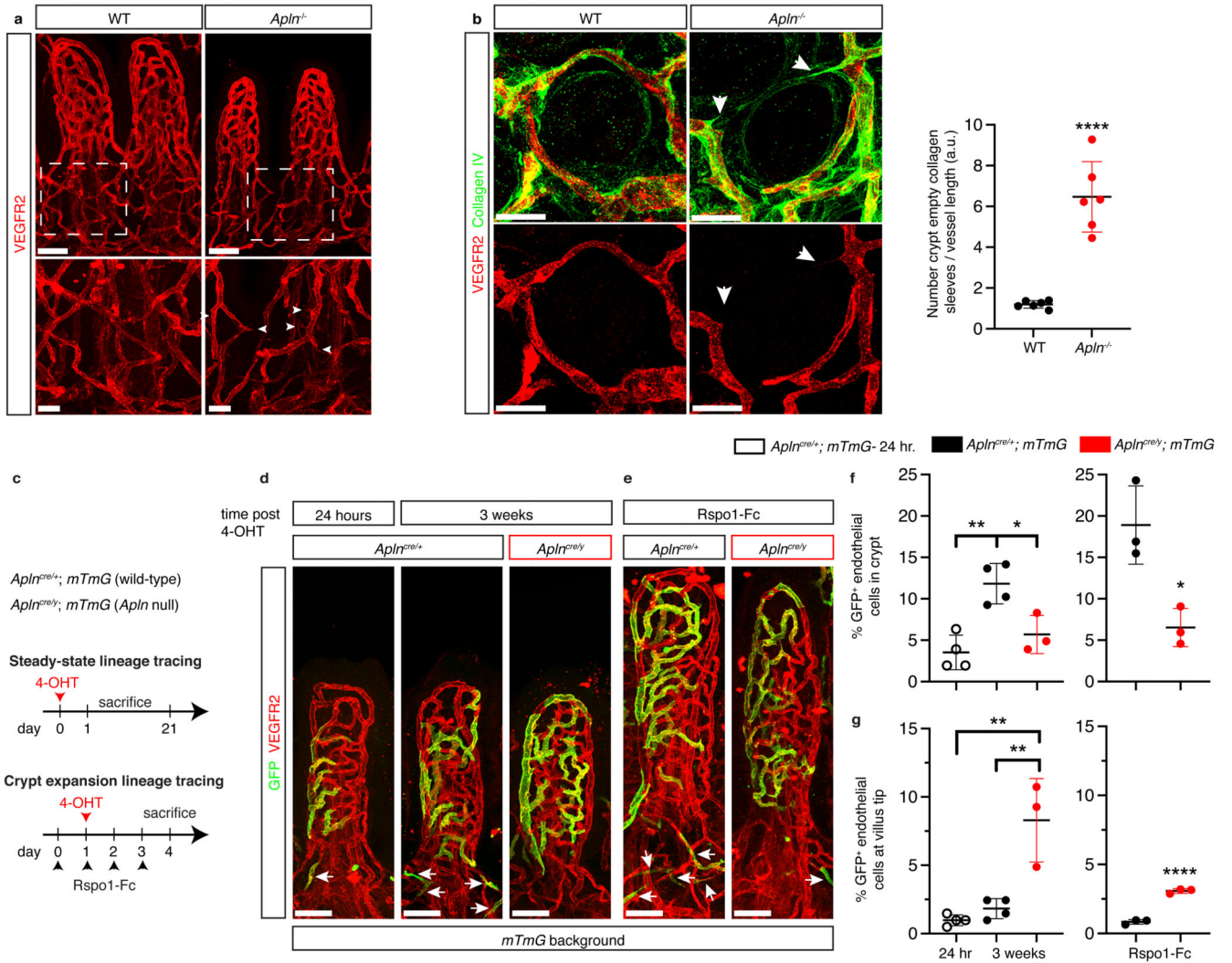


Fig. 5. Apelin-mediated crypt-ward endothelial migration maintains crypt venous capillary patency.

(a) Increased number of blind-ended crypt blood vessels in *Apln*^{-/-} mice. Insets: blind-ended crypt vessels (arrowheads). Staining for VEGFR2 (red). Representative of at least 3 independent experiments. (b) Increased empty collagen sleeves (green, collagen IV) in crypt vessels (red, VEGFR2) of *Apln*^{-/-} mice. Quantification of number of empty collagen sleeves per crypt vessel length ($p < 0.0001$, $n = 6$ mice). (c) Experimental setup for *AplnCreERT2*; *mTmG* lineage tracing during both steady-state and Rspo1-Fc-mediated crypt expansion. The CreERT2 cassette is knocked-in to the *Apln* located on the X chromosome rendering *AplnCreERT2* females and males *Apln*-proficient and -deficient, respectively. (d, e) Lineage-traced GFP⁺ endothelial cells in *AplnCreERT2*; *mTmG* mice migrate to the crypts. Whole-mount immunostaining for intestinal vessels (red, VEGFR2) and GFP⁺ endothelial cells (green) after (d) 24 hours or 3 weeks at steady-state or (e) 4 days of Rspo1-Fc treatment. (f, g) Quantification of the % of GFP⁺ endothelial cells (f) in crypt vessels (left, $p = 0.0026$ *Apln*^{Cre/+}; *mTmG* 24 hr control vs *Apln*^{Cre/+}; *mTmG* 3 week; $p = 0.0232$ *Apln*^{Cre/+}; *mTmG* 3 week vs *Apln*^{Cre/y}; *mTmG* 3 week; right, $p = 0.0153$

Rspo1-Fc treated *Apln*^{Cre/+}; *mTmG* 4 day vs Rspo1-Fc treated *Apln*^{Cre/y}; *mTmG* 4 day) or (g) at the villus tip (left, p=0.001 *Apln*^{Cre/+}; *mTmG* 24 hr control vs *Apln*^{Cre/y}; *mTmG* 3 week; p=0.0023 *Apln*^{Cre/+}; *mTmG* 3 week vs *Apln*^{Cre/y}; *mTmG* 3 week; right, p<0.0001 Rspo1-Fc treated *Apln*^{Cre/+}; *mTmG* 4 day vs Rspo1-Fc treated *Apln*^{Cre/y}; *mTmG* 4 day (n = 4 *Apln*^{Cre/+}; *mTmG* 24 hr control mice, n=4 *Apln*^{Cre/+}; *mTmG* 3 week mice; n=3 *Apln*^{Cre/y}; *mTmG* 3 week mice; n=3 Rspo1-Fc treated *Apln*^{Cre/+}; *mTmG* 4 day mice and n=3 Rspo1-Fc treated *Apln*^{Cre/y}; *mTmG* 4 day mice)). Scale bars: 50 μ m: a, d, e; 20 μ m: a (inset), b. All data are shown as mean \pm SD. *P <0.05, **P < 0.01, ***P < 0.001, ****<0.0001 2-tailed unpaired Student's t test or one-way ANOVA with Bonferonni's correction (f, g; left).

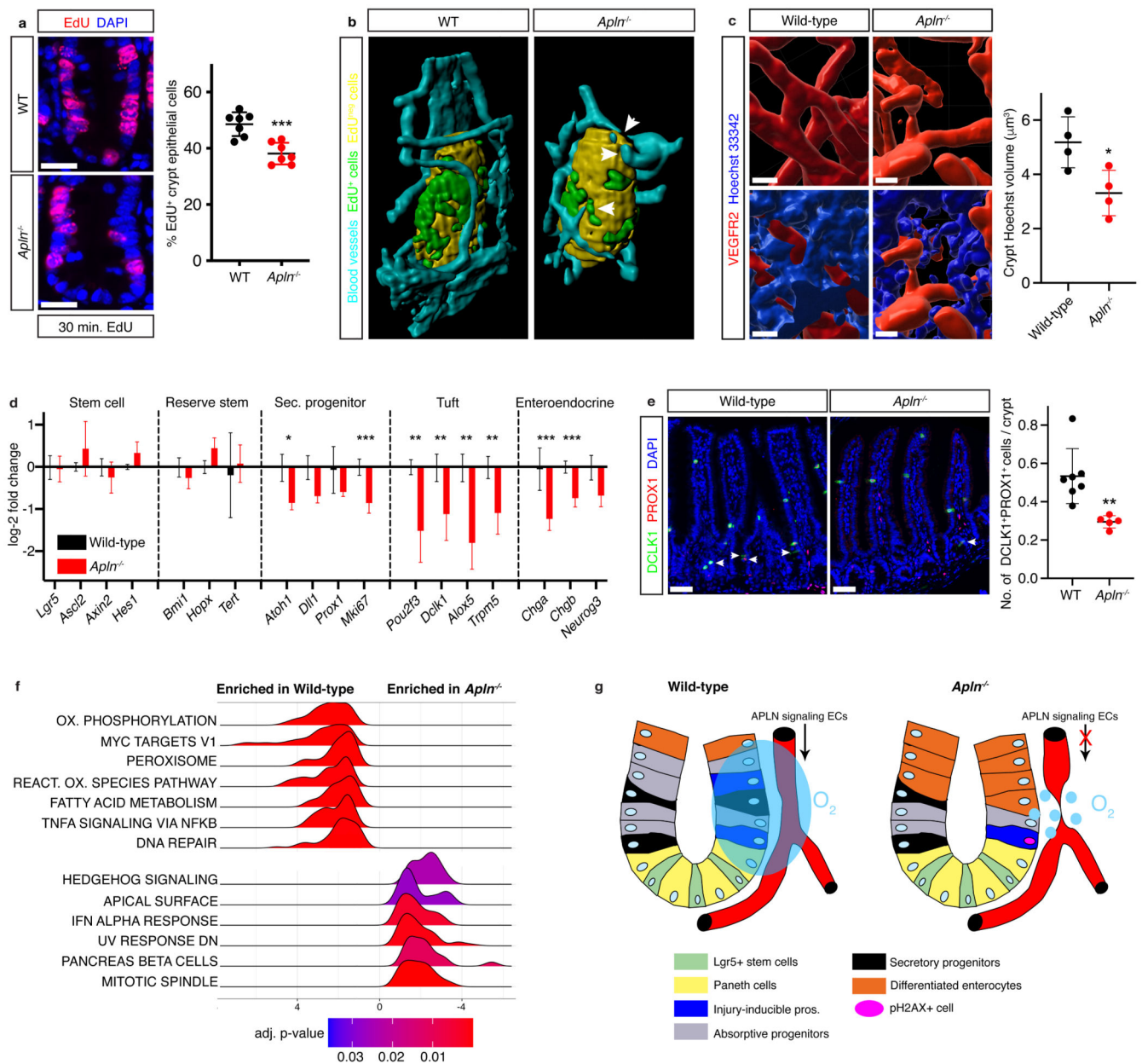


Fig. 6. Apelin is necessary for crypt perfusion and progenitor cell maintenance.

(a) Decreased proliferation of crypt stem/progenitor cells in *Apln*^{-/-} mice. Staining for EdU (red) and DNA (blue). Quantification of percentage EdU⁺ crypt epithelial cells in control and *Apln*^{-/-} mice ($p=0.0004$, $n=7$ mice). (b) 3D reconstruction of EdU⁺ (green), EdU^{neg} crypt epithelial cells (yellow) and pericryptal vessels (cyan) from control and *Apln*^{-/-} mice. Arrowheads indicate EdU^{neg} epithelial cells where vessel regression occurred. (c) Decreased perfusion of *Apln*^{-/-} intestinal crypts. 3D reconstruction of crypt blood vessels (red, VEGFR2) and perfused Hoechst 33342 (blue). Quantification of Hoechst volume around wild-type or *Apln*^{-/-} crypt vessels ($p=0.0248$, $n=4$ mice). (d) Secretory progenitor- and differentiated secretory-specific gene expression is decreased in *Apln*^{-/-} crypt epithelial cells. Average log₂-fold change of indicated gene expression from bulk RNAseq of sorted

wild-type and *Apln*^{-/-} CD44⁺ crypt epithelial cells (n=3 mice, WT vs *Apln*^{-/-}, p values: 0.0401, *Atoh1*: <0.0001, *Mki67*; 0.0027, *Pou2f3*; 0.0044, *Dclk1*; 0.002, *Alox5*; 0.0047, *Trpm5*; <0.0001, *Chga*; 0.0002, *Chgb*). (e) Decreased number of DCLK1⁺PROX1⁺ crypt epithelial cells in *Apln*^{-/-} crypts. Paraffin section immunostaining for DCLK1 (green) and PROX1 (red) in wild-type and *Apln*^{-/-} mice; blue, DAPI. Quantification of the number of DCLK1⁺PROX1⁺ cells/crypt in wild-type and *Apln*^{-/-} mice (p=0.0048, n=7 WT mice, n=5 *Apln*^{-/-} mice). (f) GSEA for Hallmark pathways for genes differentially regulated between wild-type and *Apln*^{-/-} crypt epithelial cells. (g) Model for APLN-mediated control of crypt vessel patency and secretory progenitor cell survival. APLN⁺ endothelial cells migrate at steady-state and expansion to the crypts in an APLN-dependent fashion. This migration maintains crypt vessel patency and tissue perfusion allowing the survival of crypt epithelial cells. Scale bars: 50 μm: e; 20 μm: a; 10 μm: c. All data are shown as mean ± SD. *P < 0.05, **P < 0.01, ***P < 0.001, 2-tailed unpaired Student's t test.

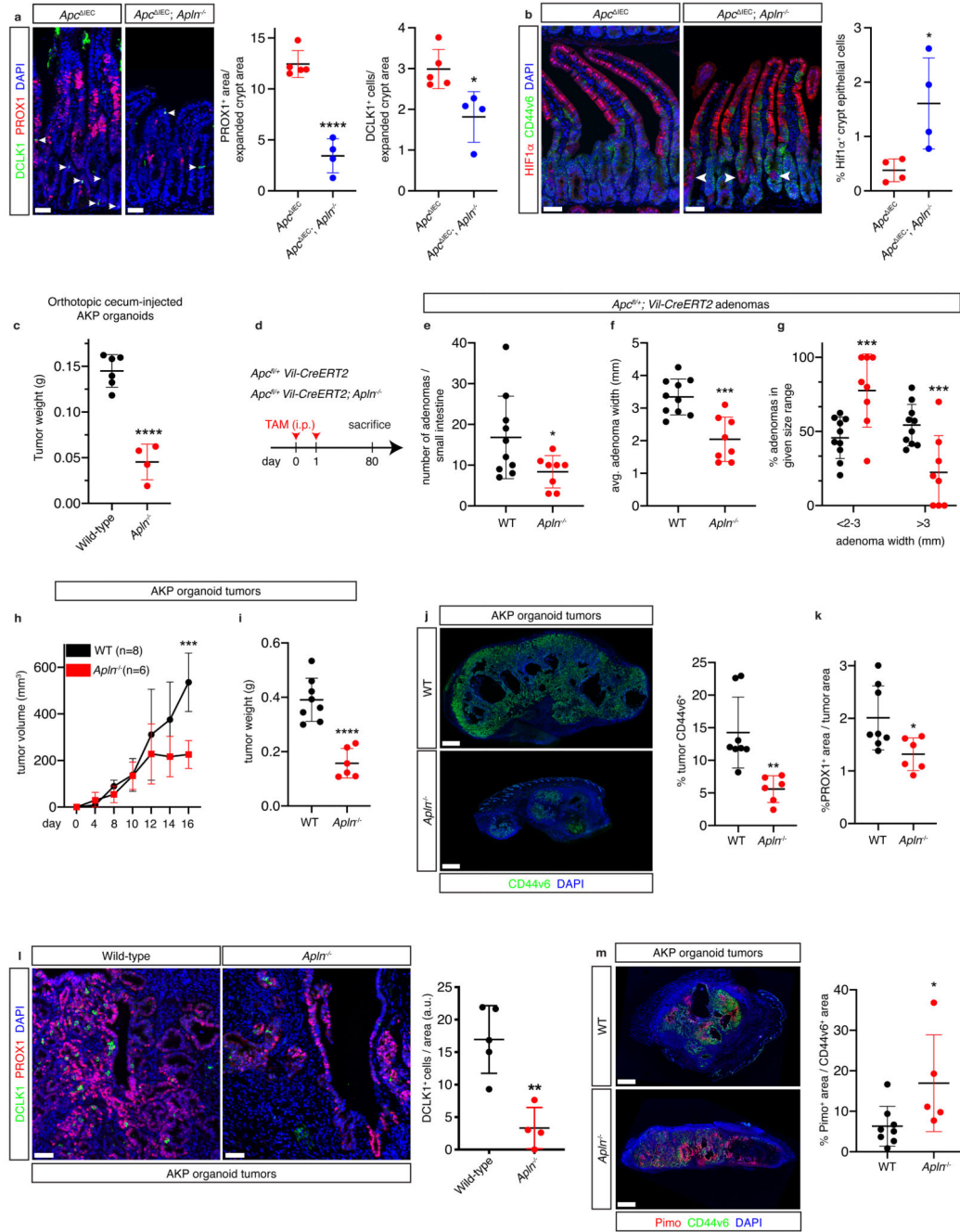


Fig. 7. APLN promotes Wnt^{high} CRC growth by ensuring progenitor cell normoxia.

(a) Decreased number of PROX1⁺ progenitor cells during acute crypt expansion. Paraffin section immunostaining of PROX1 (red) and DCLK1 (green) in *Apc^{IEC}* and *Apc^{IEC}; Aplin^{-/-}* mice; arrowheads, DCLK1⁺ cells; blue, DNA. Quantification of percentage PROX1⁺ area and number of DCLK1⁺ cells / crypt area in *Apc^{IEC}* and *Apc^{IEC}; Aplin^{-/-}* mice (left, p < 0.0001; right, p = 0.0148; n = 5 *Apc^{IEC}* and n = 4 *Apc^{IEC}; Aplin^{-/-}* mice). (b) Increased progenitor hypoxia in *Apc^{IEC}; Aplin^{-/-}* mice. Paraffin section immunostaining of CD44v6 (green) and HIF1α (red) in *Apc^{IEC}* and *Apc^{IEC}; Aplin^{-/-}* mice; blue, DNA.

Quantification of percentage HIF1 α ⁺ crypt epithelial cells in *Apc*^{IEC} and *Apc*^{IEC}; *Apln*^{-/-} mice (p=0.0292, n=4 mice). (c) AKP tumor organoids were injected orthotopically into cecae of wild-type and *Apln*^{-/-} mice and allowed to grow for 9 weeks. Quantification of the orthotopic tumor weight (p<0.0001, n=6 tumors in WT mice and n=4 tumors in *Apln*^{-/-} mice). (d-g) APLN promotes expansion but not initiation of Wnt^{high} adenomas. (d) *Apc*^{fl/+}; *Vil-CreERT2* and *Apc*^{fl/+}; *Vil-CreERT2*; *Apln*^{-/-} mice were injected with tamoxifen for two consecutive days and tumors were allowed to grow for 80 days. (e-g) Quantification of the (e) number of adenomas/small intestine (p=0.042), (f) adenoma width (p=0.004), and (g) binned adenoma size (p=0.0065; n=10 WT mice and n=8 ; *Apln*^{-/-} mice). (h, i) Apelin deficiency reduces subcutaneous AKP organoid tumor growth. AKP (h) tumor volume (day 16, p=0.0001) and (i) weight in control and *Apln*^{-/-} mice (p<0.0001; n=8 tumors in WT mice and n=6 tumors in *Apln*^{-/-} mice). (j-l) Apelin deficiency reduces number of progenitor cells in AKP tumors. Staining for progenitor markers (j) CD44v6 (green) or (l) DCLK1 and PROX1 in control and *Apln*^{-/-} mice; DNA (blue). Quantification of (j) CD44v6⁺ (p=0.0031; n=8 tumors in WT mice and n=6 tumors in *Apln*^{-/-} mice) (k) PROX1⁺ (p=0.0265; n=8 tumors in WT mice and n=6 tumors in *Apln*^{-/-} mice) or (l) DCLK1 areas in AKP tumor organoids grown in control and *Apln*^{-/-} mice (p=0.0026; n=5 tumors in WT mice and n=4 tumors in *Apln*^{-/-} mice). (m) Apelin deficiency increases progenitor cell hypoxia in AKP organoid tumors. Paraffin section immunostaining for pimonidazole (red, Pimo) and CD44v6 (green) in subcutaneous AKP tumors grown in control and *Apln*^{-/-} mice. Percentage of pimonidazole area in CD44v6⁺ areas of AKP tumors grown in control and *Apln*^{-/-} mice (p=0.0441; n=8 tumors in WT mice and n=5 tumors in *Apln*^{-/-} mice). Scale bars: 1 mm: j, m; 50 μ m: a, b, l. All data are shown as mean \pm SD. **P* < 0.05, ***P* < 0.01, ****P* < 0.001, *****P* < 0.0001 2-tailed unpaired Student's *t* test.